Geological Society of America
Special Paper 402
2006

The San Pedro–Cerro Grande volcanic complex (Nayarit, México): Inferences on volcanology and magma evolution

Chiara M. Petrone†
Dipartimento di Scienze della Terra, Università degli Studi di Firenze, Via Giorgio La Pira, 4, I-50121, Firenze, Italy

Lorella Francalanci
Dipartimento di Scienze della Terra, Università degli Studi di Firenze, Via Giorgio La Pira, 4, I-50121, Firenze, Italy, and *Sezione di Firenze, Consiglio Nazionale delle Ricerche, Istituto di Geoscienze e Georisorse, Via Giorgio La Pira 4, I-50121, Firenze, Italy*

Luca Ferrari
Centro de Geociencias, Universidad Nacional Autónoma de México, Campus Juriquilla, Apdo. Postal 1-742, 76100, Querétaro, México

Peter Schaaf
Instituto de Geofísica, Universidad Nacional Autónoma de México, Del. Coyoacan, 04510, México D.F., México

Sandro Conticelli
Dipartimento di Scienze della Terra, Università degli Studi di Firenze, Via Giorgio La Pira, 4, I-50121, Firenze, Italy, and *Sezione di Firenze, Consiglio Nazionale delle Ricerche, Istituto di Geoscienze e Georisorse, Via Giorgio La Pira 4, I-50121, Firenze, Italy*

ABSTRACT

This study focuses on two issues that are still a matter of debate in subduction zones, particularly in western México: (1) the close association within the same volcanic complex of typical amphibole-free andesites to rhyolites and amphibole-bearing andesites to rhyolites, characteristic of the hydrated front of the Mexican arc; and (2) the occurrence of bimodal magmatism without evidence for interaction between mafic and intermediate to silicic magmas, which are in addition characterized by different petrogenetic affinities. Our case study is the San Pedro–Cerro Grande volcanic complex, a Quaternary silicic to intermediate dome complex located in western Mexico. Volcanic activity has been divided into two periods. In the middle Pleistocene, andesitic to dacitic magmas were emplaced along WNW-trending faults in the southern portion of the complex. The Las Cuevas pyroclastic sequence (older than ca. 500 ka) was emplaced during this episode, most likely from a local source. This first period of activity ended before ca. 280 ka with the emplacement of the Cuastecomate Plinian deposit, which is related to the formation of the San Pedro caldera, an ~4-km-wide subcircular depression that is today partially buried by younger volcanic products. During the second period of activity (ca. 280–30 ka), rhyolitic and dacitic domes were

---

†E-mail: chiara.petrone@geo.unifi.it.

Petrone, C.M., Francalanci, L., Ferrari, L., Schaaf, P., and Conticelli, S., 2006, The San Pedro–Cerro Grande volcanic complex (Nayarit, México): Inferences on volcanology and magma evolution, *in* Siebe, C., Macías, J.L., and Aguirre-Díaz, G.J., eds., Neogene-Quaternary continental margin volcanism: A perspective from México: Geological Society of America Special Paper 402, Penrose Conference Series, p. 65–98, doi: 10.1130/2006.2402(03). For permission to copy, contact editing@geosociety.org.

mostly emplaced along the caldera rim and inside the caldera. In addition, hawaiites and mugearites built the Amado Nervo shield volcano on the caldera rim.

Intermediate- to high-silica lava and pyroclastic rocks are subalkaline, whereas the Amado Nervo mafic lavas are transitional toward the alkaline series (Na-alkaline). No genetic relationships have been found between subalkaline and transitional Na-alkaline rocks, which are thought to represent different batches of magma from different mantle sources. Petrographic, geochemical, and isotopic variations observed in the transitional Na-alkaline Amado Nervo lavas point to a parental magma from a mantle melt that underwent limited olivine separation during its ascent to the surface. Among subalkaline rocks, two groups showing contrasting petrographical and geochemical features are recognized based on the presence of amphibole. Amphibole-bearing intermediate to silicic rocks are characterized by lower Ce and other incompatible trace element contents and lower $^{87}Sr/^{86}Sr$ (0.70382–0.70401) compared to amphibole-free rocks (0.70411–0.70424). On the basis of petrological characteristics, the two groups of magmas are interpreted to have evolved in two different magmatic reservoirs under different pressures and water contents in the mid-upper crust. Both groups of magmas were differentiated by open-system processes. We propose that assimilation and equilibrium crystallization (AEC) processes account for the amphibole-bearing rocks. Hotter and less evolved magmas interacted to a higher degree with the crust than the more evolved and colder magmas. This produced the observed higher $^{87}Sr/^{86}Sr$ in the less differentiated rocks of the amphibole-bearing group. On the other hand, amphibole-free rocks have chemical and isotopic characteristics that can be modeled by assimilation and fractional crystallization (AFC) processes. All data suggest that the two groups of subalkaline rocks have been generated by a common parental hydrous magma, but evolved in two different reservoirs. Amphibole-bearing magmas underwent amphibole fractionation in a mid-upper crustal reservoir and show assimilation of two types of basement: one akin to Oaxaquia and another akin to the Guerrero terrane. Amphibole-free magma only shows assimilation of an Oaxaquia-type basement.

Keywords: subalkaline, Na-alkaline magmatism, crustal contamination, amphibole-bearing, amphibole-free magmas, water saturated magma, Trans-Mexican Volcanic Belt.

INTRODUCTION

The occurrence within the same volcanic complex of coeval bimodal magmatism belonging to different magmatic series with no evidence of interaction between them is still a matter of debate and has implications for understating how magmatic systems work. Moreover, amphibole-free and amphibole-bearing andesitic to rhyolitic rocks are commonly found in the western Mexican Volcanic Belt. The former are typical for volcanic activity in the rear part of the arc, whereas the latter are commonly associated with magmatism in the hydrated front of the arc. Thus, their occurrence within a single volcanic complex, in the rear part of the arc, gives insights on the role played by amphibole fractionation and water budgets in this important sector of the arc. The San Pedro–Cerro Grande volcanic complex is constituted by domes and a small shield volcano, with bimodal activity that produced completely distinct types of magmas within a restricted area and a short period of time. The San Pedro–Cerro Grande volcanic complex is also characterized by the presence of amphibole-free and amphibole-bearing intermediate to silicic rocks, thus representing a good place for studying the evolution of complex magmatic systems.

The San Pedro–Cerro Grande volcanic complex is located in the San Pedro–Ceboruco graben, part of the Tepic-Zacoalco rift in western México (Fig. 1) (Ferrari et al., 2003). Late Miocene to Quaternary magmatism in this region is part of the western Trans-Mexican Volcanic Belt (Fig. 1), which is characterized by the coexistence of subduction-related and intraplate-type magmatic rocks (e.g., Nelson and Carmichael, 1984; Nelson and Livieres, 1986; Verma and Nelson, 1989a, 1989b; Righter et al., 1995; Ferrari et al., 2001; Petrone et al., 2003). The western sector of the Trans-Mexican Volcanic Belt is related to subduction of the

Figure 1. Schematic map of western México showing the geodynamic setting and the location of the studied area. Symbols: gray field—Trans-Mexican Volcanic Belt; TZR—Tepic-Zacoalco rift; ChR—Chapala rift; CR—Colima rift; G—Guadalajara; T—Tepic (modified from Petrone et al., 2003).

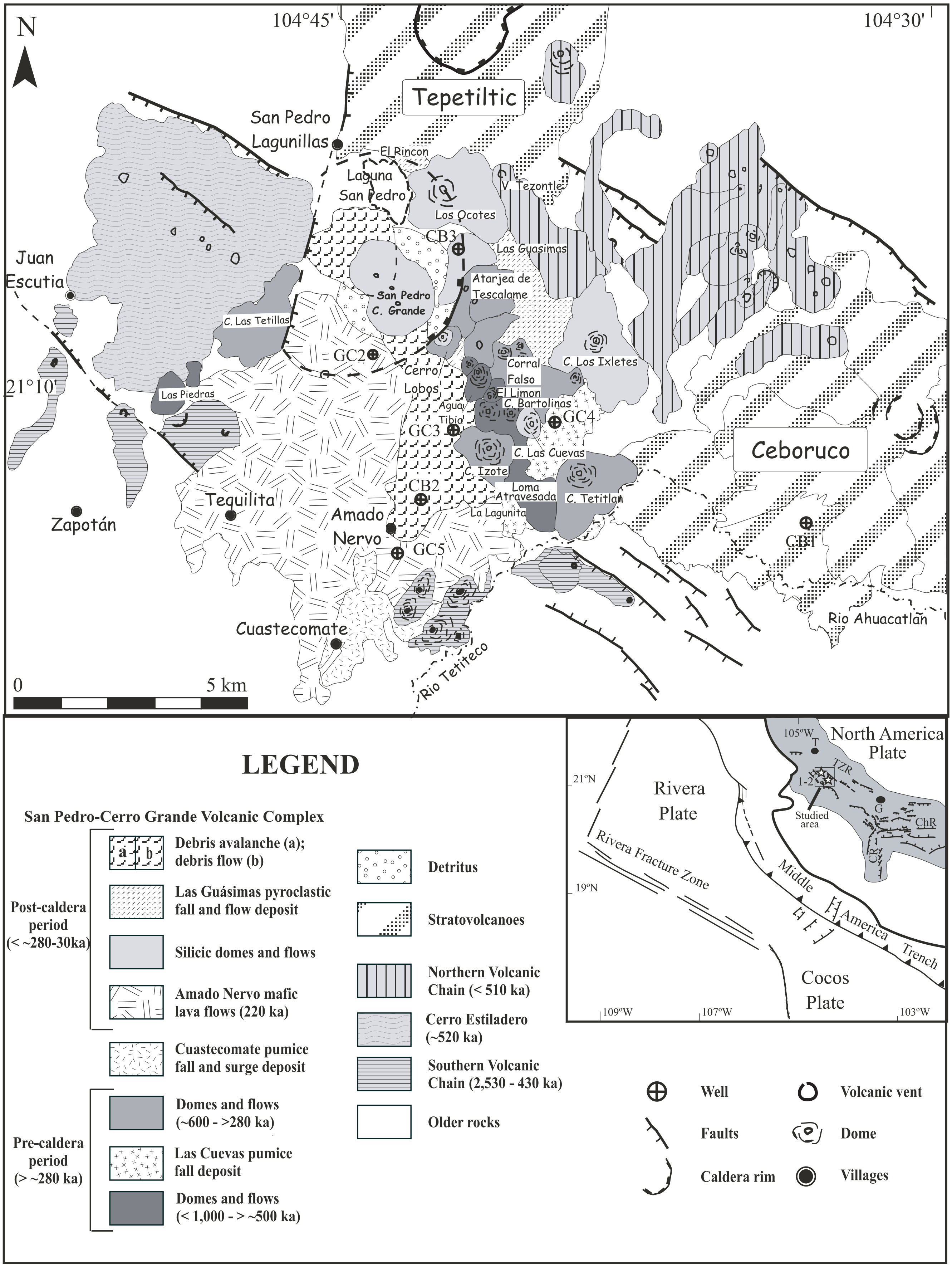
N
104°45'
104°30'
21°10'
Tepetiltic
San Pedro Lagunillas
El Rincon
Laguna San Pedro
Los Ocotes
V. Tezontle
Las Guasimas
CB3
Juan Escutia
San Pedro C. Grande
Atarjea de Tescalame
C. Las Tetillas
GC2
Cerro Lobos
Corral Falso
C. Los Ixletes
El Limon
C. Bartolinas
Las Piedras
Agua Tibia
GC4
GC3
C. Las Cuevas
Ceboruco
C. Izote
Loma Atravesada
C. Tetitlan
CB2
La Lagunita
Tequilita
Zapotán
Amado Nervo
GC5
CB1
Rio Ahuacatlan
Cuastecomate
Rio Tetiteco
0
5 km
LEGEND
San Pedro-Cerro Grande Volcanic Complex
Post-caldera period (< ~280-30ka)
a
b
Debris avalanche (a); debris flow (b)
Las Guásimas pyroclastic fall and flow deposit
Silicic domes and flows
Amado Nervo mafic lava flows (220 ka)
Cuastecomate pumice fall and surge deposit
Pre-caldera period (> ~280 ka)
Domes and flows (~600 - >280 ka)
Las Cuevas pumice fall deposit
Domes and flows (< 1,000 - > ~500 ka)
Detritus
Stratovolcanoes
Northern Volcanic Chain (< 510 ka)
Cerro Estiladero (~520 ka)
Southern Volcanic Chain (2,530 - 430 ka)
Older rocks
Well
Faults
Caldera rim
Volcanic vent
Dome
Villages
21°N
19°N
109°W
107°W
105°W
103°W
Rivera Plate
Rivera Fracture Zone
North America Plate
T
TZR
1-2
Studied area
G
ChR
CR
Middle America Trench
Cocos Plate

young Rivera microplate beneath the North American plate (Fig. 1), and intra-arc extension is a common feature of this sector of the belt (Ferrari and Rosas-Elguera, 2000). Extensional faulting began in the late Miocene in connection with the initial rifting of the southern Gulf of California (Ferrari, 1995) and continued in Pliocene-Quaternary times, likely because of plate-boundary forces (Rosas-Elguera et al., 1996; Ferrari and Rosas-Elguera, 2000).

The San Pedro–Ceboruco graben is a complex, WNW-ESE–striking extensional basin constituted by the Compostela graben to the west, and by the Ceboruco asymmetric graben to the east (Ferrari et al., 2003). Quaternary volcanism in the San Pedro–Ceboruco graben consists of at least four different volcanic systems: (1) alignments of cinder cones and domes developed on the northern and the southern edges of the graben, respectively (i.e., northern and southern volcanic chains); (2) Ceboruco stratovolcano, located in the southeastern sector of the graben; (3) Tepetiltic stratovolcano, located just north of the graben; and (4) the San Pedro–Cerro Grande volcanic complex proper, located in the central sector of the graben.

Although extensive geochronological studies have focused on the products of the San Pedro–Cerro Grande volcanic complex (e.g., Gastil et al., 1978; Ferrari et al., 2000; Petrone et al., 2001; Frey et al., 2004a), only a few papers have dealt with the volcanology (Castillo and De La Cruz, 1992; Ferrari et al., 2003) and petrology (Petrone et al., 2003) of its products to help understand the detailed history of the volcanic complex. Petrone et al. (2003) restricted their study to mafic transitional rocks of the San Pedro–Cerro Grande volcanic complex. In the present paper, we report detailed statigraphical, mineralogical, geochemical, and isotopic data on samples covering the entire period of activity of the San Pedro–Cerro Grande volcanic complex. Our primary objective is to describe magma evolution of the complex and its relationships to tectonic features and volcanic activity.

VOLCANIC STRATIGRAPHY

The San Pedro–Cerro Grande volcanic complex consists of coalesced domes, with minor lava flows and pyroclastic products. A caldera rim can be observed in the northeastern portion of the complex and is inferred to be buried or destroyed elsewhere (Castillo and De La Cruz, 1992; Ferrari et al., 2003). The emplacement of the three overlapping San Pedro–Cerro Grande domes inside the inferred caldera, and a small dome on its caldera rim (Fig. 1), closed the volcanic activity. Highly viscous block lava flows of variable thickness are also found associated with the domes. Both domes and lava flows contain rounded centimeter-sized magmatic enclaves, which rarely reach 10 cm in diameter and are slightly darker in color than the host rock.

Reconstruction of the eruptive history of the San Pedro–Cerro Grande volcanic complex on the basis of field data alone is difficult to achieve, given the abundant vegetation. The volcanic stratigraphy was determined on the basis of field work combined with numerous radiometric ages (Ferrari et al., 2000; Petrone et al., 2001; Frey et al., 2004a) and by subsurface data obtained from geothermal drilling by the Comisión Federal de Electricidad (Ferrari et al., 2003). Volcanic rocks of the San Pedro–Cerro Grande volcanic complex (Fig. 1) are bounded by older volcanic rocks and monogenetic centers to the west and south. Furthermore, they are interfingered with volcanic products from Volcán Tepetiltic and monogenetic centers of the Northern volcanic chain to the north, and covered by recent volcanic products from Volcán Ceboruco to the east. Most San Pedro–Cerro Grande volcanic complex vents are aligned broadly along WNW-ESE–trending lineaments, which parallel the main tectonic structures bounding the San Pedro–Ceboruco graben and the Tepic-Zacoalco rift (Ferrari and Rosas Elguera, 2000).

Volcanic activity in the San Pedro–Cerro Grande volcanic complex is limited to the Quaternary. On the basis of field and geochronological data, Ferrari et al. (2003) divided its activity into three main periods, separated by Plinian deposits (Fig. 2). In this section, we revise the stratigraphy summarized in Ferrari et al. (2003) in the light of recent geochronological data (Frey et al., 2004a, 2004b). We also discuss the source of Plinian deposits and evidence for the existence of the San Pedro caldera.

First Period of Activity (Middle Pleistocene)

San Pedro–Cerro Grande volcanic complex volcanism began with the emplacement of several lava domes in the southern part of the complex (Fig. 1). In addition, several dacitic lava flows, found up to 288 m deep beneath the southern portion of the San Pedro–Cerro Grande volcanic complex in the CB2 drill hole (Fig. 1) (Ferrari et al., 2003), are considered part of this initial activity. The Las Cuevas pyroclastic deposit (see next section) was emplaced during this period after the extrusion of Cerro Bartolinas, Cerro Agua Tibia, and Cerro El Limón domes, and of Cerro Las Piedras and Loma Atravesada lava flows. Cerro Las Piedras has been dated at 821 ± 25 ka by ^{40}Ar/^{39}Ar (Frey et al., 2004a) dating. Cerro Bartolinas and an unnamed dome to the NW have been dated at 1400 ± 300 ka and 1600 ± 300 ka, respectively, by conventional K-Ar dating (Ferrari et al., 2000). In other cases, where more precise ^{40}Ar/^{39}Ar dates are available for the same lavas (Frey et al., 2004a), these K-Ar ages, obtained ~15 yr ago at the Instituto Mexicano del Petróleo (IMP), proved to be systematically older. In addition, Frey et al. (2004a) obtained an age of 623 ± 91 ka for an unnamed dome just to the NW of the dome dated at 1600 ka by Ferrari et al. (2000) (Fig. 1). Consequently, although no ^{40}Ar/^{39}Ar age is available for the domes of this initial phase of activity, they are considered here to be middle Pleistocene in age.

Several domes and associated viscous lava flows were emplaced after the effusion of the Las Cuevas deposit. These domes are Cerro Las Cuevas, Cerro Lobos, Cerro Izote, Cerro Tetitlán, and Cerro Las Tetillas (Fig. 1). In addition, a small vent in Las Guásimas area produced several intermediate lava flows forming the small volcanic cone of Atarjea de Tescalame (Fig. 1). According to the ^{40}Ar/^{39}Ar geochronology of Frey et al. (2004a),

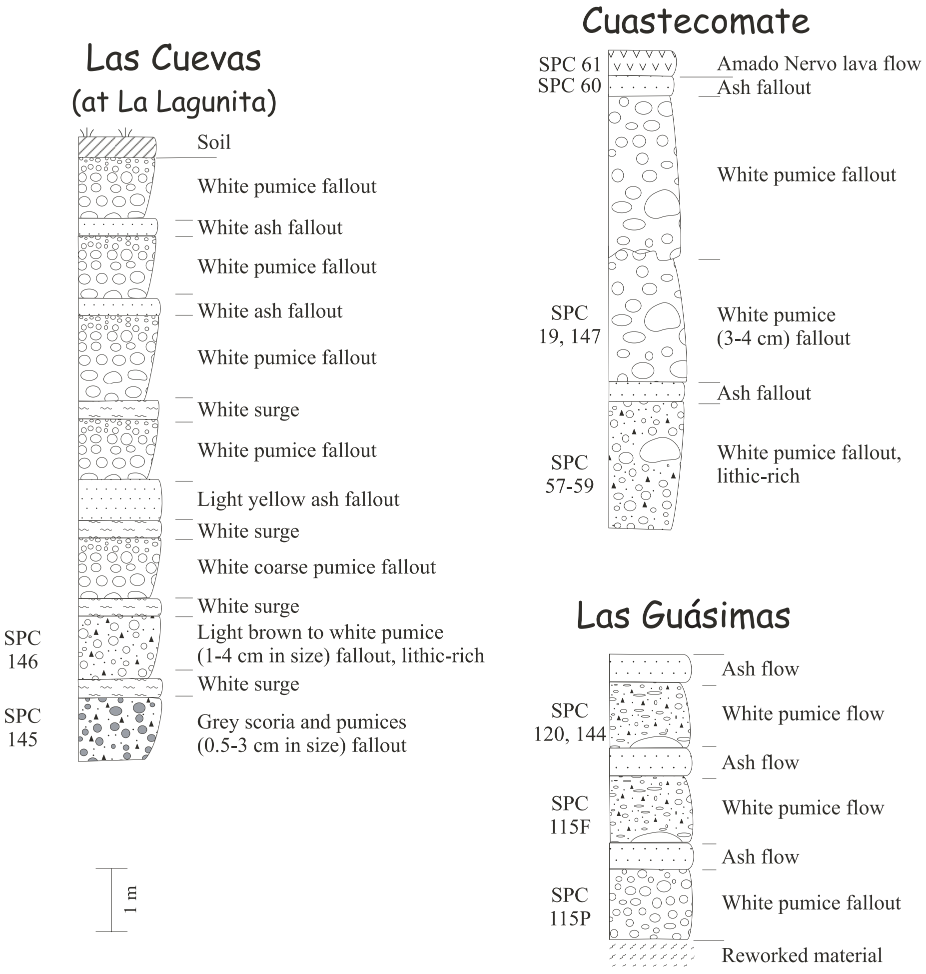

Figure 2. Stratigraphic columns of the pyroclastic deposits associated with the San Pedro–Cerro Grande volcanic activity, as reconstructed in this study. Each column represents the typical pyroclastic sequence based on stratigraphic data found at different localities. The stratigraphic levels from which samples (SPC) were collected are also indicated. Samples SPC105 and 129 from the pumice fall of the Las Cuevas deposit are not reported here given their uncertain attribution to a specific level of the reconstructed sequence.

the domes were erupted between ca. 623 and ca. 441 ka. In the case of the Cerro Lobos dome, the previous K-Ar age of ca. 610 ka obtained at IMP (Ferrari et al., 2000) is consistent with the K-Ar age of 610 ka obtained by Petrone et al. (2001) and with the ^{40}Ar/^{39}Ar age of ca. 601 ka obtained by Frey et al. (2004a). The Atarjea de Tescalame andesites were also dated by the K-Ar method at IMP and were found to be 530 ka (Ferrari et al., 2000), an age consistent with the fact that these flows partly cover the Cerro Lobos domes.

Las Cuevas Pyroclastic Deposit

The Las Cuevas pyroclastic deposit consists of a pyroclastic sequence, well exposed in the Las Cuevas area, where it covers some of the above-described early domes and lava flows of the first period (Fig. 1). It consists of pumice fallout deposits alternating with thin layers of pyroclastic-surge and ash fallout deposits, characterized by white, highly vesiculated aphyric pumice clasts, with maximum sizes of 10 cm, and abundant dacitic lava lithics (Fig. 2). At Las Cuevas, the basal portion of this unit is constituted by a welded pyroclastic flow deposit with abundant andesitic to dacitic lava lithic fragments up to 50 cm in diameter of unknown provenance. The upper portion is composed of a pumice fallout deposit with white aphyric pumices and few small dacitic lithics. The Las Cuevas deposit can be followed up to La Lagunita site (Fig. 1), where at least seven different layers of pumice fallout separated by ash fallout and surge deposits were recognized (Fig. 2), with a total exposed thickness of 10 m. The basal pumice fallout deposit contains slightly darker aphyric pumices and is rich in lithic fragments of dacitic and andesitic lavas and low-grade metamorphic rocks. The maximum size of pumice clasts increases upsection. Pumice fragments are also inversely graded within single layers. The base of the deposit is not exposed, but its maximum thickness was found at the geothermal well GC4 at Las Cuevas (Fig. 1), where dacitic lavas were encountered below a 36-m-thick pile of the Las Cuevas pumice deposit (Ferrari et al., 2003).

The Las Cuevas deposit was not dated directly, but the sequence covers Cerro Bartolinas and Loma Atravesada (Fig. 1), which are most likely middle Pleistocene in age (see previous section). Furthermore, the sequence underlies the Cerro Las Cuevas dome, dated at 780 ± 160 ka by the conventional K-Ar method at IMP (Ferrari et al., 2000). The Cerro Izote and Cerro Tetitlán domes, located to the west and to the east of Loma Atravesada, respectively (Fig. 1), are not covered by the Las Cuevas deposit. A pumice deposit, probably related to the Las Cuevas, is actually exposed at the base of Tetitlán dome. Cerro Izote has been dated at ca. 441 ± 71 ka and Cerro Tetitlán at ca. 500 ± 56 ka by the ^{40}Ar/^{39}Ar method (Frey et al., 2004a). Therefore, if we discard the ca. 780 ka age obtained at IMP for the Las Cuevas dome, the deposit should be older than ca. 500 ka.

The source of the Las Cuevas deposit is not easy to establish. Among the possible sources are the San Pedro caldera (Castillo and De La Cruz, 1992; Ferrari et al., 2003), the Tepetiltic caldera (DeRemer, 1986; Frey et al., 2004b), the Ceboruco caldera (Nelson, 1980; Gardner and Tait, 2000), and a local vent presently buried by younger dome activity. The Ceboruco caldera is unlikely to be the source, because its formation occurred only ~1000 yr ago (Nelson, 1980), and its fallout deposits are restricted to the area to the northeast of Ceboruco volcano (Gardner and Tait, 2000). The Tepetiltic caldera can be also excluded for several reasons: (1) the thickness of the pyroclastic deposits of the Tepetiltic caldera–forming eruption are reported to be less than ~10 m inside the caldera and 5 m or less at the base of Tepetiltic volcano (DeRemer, 1986). In the San Pedro Lagunillas area (Fig. 1), DeRemer (1986) reported only 3 m of pyroclastic deposits. In contrast, over 10 m of the Las Cuevas pumice deposits are exposed at La Lagunita, and a total thickness of ~36 m was encountered at the GC4 well (Ferrari et al., 2003), both located ~9 km further to the south. (2) The composition of pumices from the Las Cuevas deposits is andesitic to dacitic (Tables 1 and 2), whereas the pyroclastic deposits related to the caldera-forming eruption of Tepetiltic are rhyolitic (DeRemer, 1986; Frey et al., 2004b). (3) The dominant composition of lithics in the Las Cuevas deposits is dacitic, whereas the lavas exposed along the rim of the Tepetiltic caldera are dominantly andesitic (DeRemer, 1986). (4) Last, the age of the youngest lava flow exposed along the Tepetiltic caldera rim has been dated at ca. 230 ka by Frey et al. (2004b), whereas the Las Cuevas deposit is older than ca. 500 ka. To relate the Las Cuevas deposit to the San Pedro caldera is also problematic, because, as explained later, the latter is younger than ca. 450 ka. Given these arguments and taking into account the relatively small areal distribution of the Las Cuevas pumice deposits, we consider that this deposit is probably related to the emplacement of one of the early domes in the area.

Cuastecomate Pumice Deposit

The Cuastecomate pumice deposit is a Plinian fallout deposit that consists of an alternating sequence of pumice fallout and ash fallout layers. These are capped by a 30-cm-thick ash fallout layer (Fig. 2), which is well exposed below basaltic flows of the Amado Nervo volcano near the Cuastecomate village (Fig. 1). Juvenile fragments are represented by white pumice clasts with variable crystal contents. Pumices are up to 10 cm in diameter and reversely graded. The deposit is rich in lithic fragments of dacitic, rhyolitic, and less abundant andesitic lavas, as well as low-grade metamorphic rocks and silicic hypabyssal volcanic rocks. According to the CB2 well log, ~90 m of Cuastecomate pumice deposit was found below olivine basalts of the Amado Nervo volcano (Ferrari et al., 2003). The only age constraint for the deposit stems from the overlying Amado Nervo shield volcano, which was dated at 220 ± 29 ka (Frey et al. 2004a). A pumice fallout was also found on top of the Ixletes dome (Fig. 1). This dome was dated at 264 ± 52 ka (Frey et al. 2004a), but correlation of the overlying pumice deposit with the Cuastecomate deposit is uncertain. In the following section, we explain how the Cuastecomate deposit is related to the formation of the San Pedro caldera.

San Pedro Caldera

The existence of the San Pedro caldera was originally proposed by Castillo and De La Cruz (1992) and Petrone et al. (2001), but an outline of its possible geometry was first described by Ferrari et al. (2003). The caldera is inferred to be a subcircular depression now occupied by Laguna San Pedro and San Pedro–Cerro Grande domes. The western rim could be located along an ~N-S normal fault (Fig. 1). Evidence for proposing the existence of the San Pedro caldera includes: (1) a partly preserved caldera rim bounding a topographic depression, (2) the emplacement of two of the largest volcanic centers along the inferred caldera rim, and (3) the presence of the thick Cuastecomate pumice deposit just to the south of the caldera.

The caldera rim is only partly preserved at the eastern and western edges of the depression, and has been destroyed or covered by younger volcanic products elsewhere. The eastern rim is inferred along the arched scarps that bound Cerro Lobos and Atarjea de Tescalame domes to the west. At both of these domes, the western flank is much steeper than the other flanks, indicating that it is not a primary morphologic feature. The western rim of the caldera is considered to pass along the arched scarp that bounds the Las Tetillas dome to the east. In plan view, this latter dome is clearly asymmetric, with a morphology suggesting that part of the eastern flank is missing. The vents of the Amado Nervo shield volcano and the Los Ocotes dome are located along the inferred trace of the southern and northern inferred caldera rims, respectively (Fig. 1). The northern rim is covered by pumice and ash deposits likely related to the Tepetiltic caldera. To the south, the rim is covered by the Amado Nervo volcano and the debris avalanche flow of the southern San Pedro dome (Fig. 1).

The caldera rim encircles a marked depression later filled by younger volcanic products. The CB3 well drilled close to the NE rim found ~270 m of rhyolitic flows (dated ca. 283 ka at surface by Frey et al., 2004a) followed by ~600 m of amphibole-bearing dacites, and, finally, over 1 km of a fine-grained granitoid rock (Ferrari et al., 2003). The amphibole-bearing dacites lie ~400 m lower than the top of similar rocks outside the caldera rim. The temperature at the base of the well (~700 m below sea level) approaches 300 °C (CFE, Gerencia de Proyectos Geotermoeléctricos, 1993, written communication), indicating that the

TABLE 1. LOCATIONS OF STUDIED SAMPLES (SAMPLES LISTED IN INFERRED CHRONOLOGICAL ORDER)

Sample	Locality	Lithology	Latitude (N)	Longitude (W)	Age (ka)	Comments
First Period						
SPC 123	Cerro Agua Tibia	Lava	21°08′00″	104°41′45″	un.	Amphibole-bearing dacite lava with porphyritic texture, aphyric enclave bearing
SPC 122	Cerro Agua Tibia	Lava	21°08′30″	104°41′80″	un.	Amphibole-bearing dacite lava with porphyritic texture, porphyritic enclave bearing
SPC 126	Cerro Agua Tibia	Lava	21°08′00″	104°41′30″	un.	Amphibole-bearing dacite lava with porphyritic texture, porphyritic enclave bearing
SPC 124	Cerro Bartolinas	Lava	21°07′45″	104°41′30″	un.	Amphibole-bearing andesite lava with porphyritic texture
SPC 56	Loma Atravesada	Lava	21°06′04″	104°40′73″	un.	Amphibole-bearing andesite lava with low porphyritic texture
SPC 55	Loma Atravesada	Lava	21°06′04″	104°40′73″	un.	Amphibole-bearing andesite lava with porphyritic texture
SPC 125	Cerro El Limon	Lava	21°08′00″	104°41′30″	un.	Amphibole-bearing dacite lava with porphyritic texture
GC4-74	Las Cuevas GC4 well	Lava	21°07′40″	104°39′60″	un.	Amphibole-free dacite lava with porphyritic texture
GC6-288	Amado Nervo CB2 well	Lava	21°05′90″	104°43′10″	un.	Amphibole-free dacite lava with low porphyritic texture
GC4-118	Las Cuevas GC4 well	Lava	21°07′40″	104°39′60″	un.	Amphibole-free dacite lava with low porphyritic texture
GC4-170	Las Cuevas GC4 well	Lava	21°07′40″	104°39′60″	un.	Amphibole-free dacite lava with porphyritic texture
SPC 129	Las Cuevas–Valle Verde	Pumice	21°06′50″	104°39′45″	un.	Amphibole-free dacite white pumice with aphyric texture
SPC 105	Las Cuevas–Puerta Veja	Pumice	21°05′00″	104°38′00″	un.	Amphibole-free white small (<1 cm) aphyric pumice
SPC 146	Las Cuevas–La Lagunita	Pumice	21°05′43″	104°41′31″	un.	Amphibole-free white andesite pumice with aphyric texture
SPC 145	Las Cuevas–La Lagunita	Pumice	21°05′43″	104°41′31″	un.	Amphibole-free white small (<1 cm) aphyric pumice
SPC 130	Cerro Las Cuevas	Lava	21°07′20″	104°40′00″	780(1)?	Amphibole-bearing dacite lava with porphyritic texture, porphyritic enclave bearing
SPC 117	Atarjea de Tescalame	Lava	21°10′00″	104°41′55″	674(3)–530(1)	Amphibole-free andesite lava with aphyric texture
SPC 118	Atarjea de Tescalame	Lava	21°09′55″	104°41′10″	674(3)–530(1)	Amphibole-free dacite lava with aphyric texture
SPC 139	Atarjea de Tescalame	Lava	21°10′31″	104°42′04″	674(3)–530(1)	Amphibole-free andesite lava with aphyric texture
SPC 127	Cerro Lobos	Lava	21°09′00″	104°42′40″	610(2)	Amphibole-bearing rhyolite lava with low porphyritic texture, aphyric enclave bearing
SPC 116	Corral Falso flow	Lava	21°08′35″	104°40′00″	un.	Amphibole-free dacite lava with porphyritic texture
SPC 131	Corral Falso flow	Lava	21°07′55″	104°40′20″	un.	Amphibole-free dacite lava with low porphyritic texture
SPC 108	Cerro Tetitlán	Lava	21°05′50″	104°39′25″	500(3)	Amphibole-bearing dacite lava with low porphyritic texture
SPC 132	Cerro Los Izote	Lava	21°06′00″	104°41′00″	441(3)	Amphibole-bearing andesite lava with porphyritic texture, porphyritic enclave bearing
SPC 19	Cuastecomate	Pumice	21°02′54″	104°44′94″	un.	Amphibole-bearing rhyolite pumice with vitrophyric texture
SPC 57	Cuastecomate	Pumice	21°02′78″	104°44′94″	un.	Amphibole-bearing rhyolite pumice with vitrophyric texture
SPC 58	Cuastecomate	Pumice	21°02′78″	104°44′94″	un.	Amphibole-bearing rhyolite pumice with vitrophyric texture
SPC 59a-i	Cuastecomate	Lithic	21°02′78″	104°44′94″	un.	Lithics from various lava domes
SPC 60	Cuastecomate	Ash	21°02′78″	104°44′94″	un.	White ash fallout
SPC 147a-d	Cuastecomate	Lithic	21°02′78″	104°44′94″	un.	Lithics from various lava domes

(*continued*)

TABLE 1. LOCATIONS OF STUDIED SAMPLES (SAMPLES LISTED IN INFERRED CHRONOLOGICAL ORDER) (*continued*)

Sample	Locality	Lithology	Latitude (N)	Longitude (W)	Age (ka)	Comments
Second Period						
SPC 69	San Pedro lava flow	Lava	21°11′24″	104°42′30″	283(3)	Amphibole-bearing rhyolite lava with vitrophyric texture
SPC 111	Los Ixletes Dome	Lava	21°10′05″	104°39′05″	264(3)	Amphibole-free dacite lava with low porphyritic texture, aphyric enclave bearing
SPC 112	Los Ixletes Dome	Lava	21°09′30″	104°39′15″	264(3)	Amphibole-free dacite lava with low porphyritic texture
SPC 114	Los Ixletes Dome	Lava	21°08′40″	104°39′55″	264(3)	Amphibole-free dacite lava with low porphyritic texture
SPC 24	Amado Nervo	Lava	21°03′21″	104°45′83″	220(3)	Alkalic olivine basalt low porphyritic
SPC 25	Amado Nervo	Lava	21°05′36″	104°47′74″	220(3)	Olivine hawaiite low porphyritic
SPC 61	Amado Nervo–Cuastecomate	Lava	21°02′78″	104°44′94″	220(3)	Olivine hawaiite low porphyritic
SPC 109	Amado Nervo	Lava	21°05′45″	104°41′25″	220(3)	Olivine hawaiite low porphyritic
SPC 18	Amado Nervo	Lava	21°08′75″	104°44′00″	220(3)	Olivine hawaiite low porphyritic
SPC 64	Amado Nervo–Arrojo Hondo	Lava	21°08′33″	104°34′36″	220(3)	Olivine hawaiite low porphyritic
SPC 17	Amado Nervo	Lava	21°08′53″	104°45′51″	220(3)	Olivine hawaiite low porphyritic
SPC 20	Amado Nervo–Compostela	Lava	21°03′01″	104°45′64″	220(3)	Olivine hawaiite low porphyritic
SPC 113	Las Guásimas–Corral Falso	Pumice	21°09′05″	104°39′30″	un.	Amphibole-bearing white and gray small (<0.5 cm) pumice
SPC 115P	Las Guásimas–Corral Falso	Pumice	21°08′40″	104°39′00″	un.	Amphibole-bearing white rhyolitic pumice with hyaline texture
SPC 115F	Las Guásimas–Corral Falso	Pumice	21°08′40″	104°39′00″	un.	Amphibole-bearing white rhyolitic pumice with hyaline texture
SPC 120	Las Guásimas–San Pedro Lagunillas	Pumice	21°12′67″	104°43′31″	un.	Amphibole-bearing white crystalline pumice
SPC 144	Las Guásimas–San Pedro Lagunillas	Pumice	21°12′67″	104°43′31″	un.	Amphibole-bearing white crystalline rhyolitic pumice
SPC 23	Cerro Los Ocotes	Lava	21°11′39″	104°40′92″	100(1)(3)	Amphibole-bearing rhyolite lava with vitrophyric texture
SPC 88	Cerro Los Ocotes	Lava	21°11′43″	104°42′00″	100(1)(3)	Amphibole-bearing rhyolite lava with vitrophyric texture
SPC 62	San Pedro Dome	Debris av.	21°06′51″	104°42′37″	41(3)	Amphibole-bearing dacite debris avalanche with porphyritic texture
SPC 63	San Pedro Dome	Debris av.	21°07′76″	104°42′42″	41(3)	Amphibole-bearing dacite debris avalanche with porphyritic texture
SPC 66	San Pedro Dome	Lava	21°10′40″	104°44′98″	41(3)	Amphibole-bearing rhyolite lava with porphyritic texture
SPC 65	San Pedro Dome	Lava	21°09′87″	104°44′93″	41(3)	Amphibole-bearing rhyolite lava with porphyritic texture
SPC 67	San Pedro Dome	Lava	21°11′02″	104°44′78″	41(3)	Amphibole-bearing rhyolite lava with low porphyritic texture, aphyric enclave bearing
SPC 68	San Pedro Dome	Lava	21°11′50″	104°43′97″	41(3)	Amphibole-bearing rhyolite lava with low porphyritic texture, aphyric enclave bearing
SPC 128	Cerro Lobos	Lava	21°09′00″	104°42′40″	30(1)	Amphibole-bearing dacite lava with porphyritic texture

Note: un.—unknown age; Debri av. —debris avalanche, ? —uncertain age. Ages from: (1) Ferrari et al. (2000); (2) Petrone et al. (2001); (3) Frey et al. (2004a).

granitoid is a recent (<1 m.y. old) subvolcanic body. By contrast, the other two deep drillings in the area (CB1 and CB2) found early Pliocene basement rocks at only ~530 and ~270 m above sea level (asl), respectively (Ferrari et al., 2003). The GC2 well, drilled on the northern slope of the Amado Nervo volcano inside the caldera (Fig. 1), cut ~130 m of basaltic flows of the volcano without encountering the base. In contrast, GC5 and CB2 wells, drilled outside the caldera rim, found only ~70 and ~20 m of basaltic flows pertaining to the Amado Nervo volcano (Ferrari et al., 2003). All the above data indicate that the area encircled by the inferred caldera rim has been lowered by a few hundreds of meters. Finally, the presence of the San Pedro lake inside the caldera rim is another indication of the existence of a caldera depression.

The age of the caldera formation is not precisely known. Field observations clearly indicate that it precedes the emplacement of the ca. 220 ka Amado Nervo volcano but follows the emplacement of the ca. 450 ± 19 ka Cerro Las Tetillas dome and the ca. 610 ka Cerro Lobos dome (Petrone et al., 2001). In addition, Frey et al. (2004a) dated a rhyolitic lava inside the caldera at 283 ± 5 ka. This lava overflows the northeastern part of the caldera rim near the CB3 well (Fig. 1). Therefore, caldera formation might have occurred between ca. 450 and ca. 283 ka.

The San Pedro caldera probably formed after the Cuastecomate eruption. A possible origin of the Cuastecomate pumice deposit from Tepetiltic volcano can be ruled out, because this caldera is much younger (i.e., ca. 230 ka, Frey et al., 2004b) than San Pedro, which is older than ca. 283 ka. In addition (as mentioned before), the thickness of the Cuastecomate deposit is inconsistent with that reported for pyroclastic deposits on the flanks of Tepetiltic volcano. As in the case for the Las Cuevas deposit, the dominant composition of lithics in the Cuastecomate deposit is dacitic, which does not match with the dominantly andesitic lavas that built Tepetiltic volcano. Major- and trace-element abundances of the Cuastecomate pumices (SPC19, 57 and 58, Tables 1 and 2) are very similar to those of the first intracaldera rhyolite lavas (SPC69, Table 2; COMP3 of Frey et al., 2004a), suggesting that the latter were outpoured shortly after eruption of the pumice from the same magma chamber.

Second Period (Postcaldera Period)

Ages for the postcaldera phase of volcanic activity range between ca. 283 ka and 30 ka (Ferrari et al., 2003; Frey et al., 2004a). This phase began with the emplacement of the viscous San Pedro lava flow and the Los Ixletes dome, in the eastern part of the San Pedro–Cerro Grande volcanic complex. Frey et al. (2004a) obtained ages of 283 ka and 264 ka, respectively, for these lavas. Shortly after (220 ka, Frey et al., 2004a), the Amado Nervo lava flows were erupted from a vent located on the southern edge of the caldera rim (Fig. 1). Because of their low viscosity, these lavas flowed over the gently sloping Cuastecomate pumice deposit and reached up to 7 km to the south, forming a shield-like structure. The Amado Nervo lava flows constitute a peculiar and unique event with respect to the rest of the San Pedro–Cerro Grande volcanic complex, both in terms of emplacement dynamics and compositional characteristics.

Subsequently, the Los Ocotes dome was emplaced on the northern caldera rim (Fig. 1) at ca. 100 ka (Ferrari et al., 2000; Frey et al., 2004a), and the three massive and coalescing San Pedro–Cerro Grande domes filled the caldera at ca. 41 ka (Frey et al., 2004a). A small dome was also formed on top of Cerro Lobos (Fig. 1) at 30 ka (Ferrari et al., 2000). The San Pedro–Cerro Grande intracaldera domes are aligned along a NW-trending fracture and attain an elevation of ~2000 m asl. Two of the domes have collapsed, one to the northwest and the other to the south, producing a debris flow, which reached a distance of ~5 km to the south, and a debris avalanche to the north, which flowed some hundred meters, forming a typical hummocky topography within the caldera.

Although the third phase was mainly characterized by effusive activity, a pyroclastic deposit is found near the village of Las Guásimas to the SE and NW of Los Ocotes dome (Fig. 1). It consists of a 3-m-thick pyroclastic flow deposit underlain by a pyroclastic fallout layer. The entire sequence is ~4.5–5 m thick (Fig. 2). Juvenile fragments of the basal fall layer are white aphyric pumices less than 10 cm in size. Similar pumices of larger size also form juvenile fragments in the pyroclastic flow deposit. Capping the sequence are white and gray pumices embedded in a lithified ashy matrix. At the site of El Rincón, located just to the west of Los Ocotes dome, the pyroclastic sequence is at least 10 m thick and consists of two pumice flow deposits underlain by a block-and-ash flow deposit. Two different types of juvenile fragments are present: large (up to 30 cm in diameter) crystal-rich (hornblende, biotite plus plagioclase) white and gray pumices and small aphyric white pumices. Some streaked pumices are found, suggesting an intimate association of these two juvenile components. Abundant lithic fragments, heterogeneous in composition and size, are also found. In particular, dacitic and rhyolitic (obsidian) lithics are found along with less abundant mafic lavas. The latter probably belong to Volcán Tezontle, a basaltic andesitic cinder cone located on the eastern flank of Los Ocotes (Fig. 1). Las Guásimas deposit covers Volcán Tezontle lava flows, which were dated by Petrone et al. (2001) at 119 ka. On this basis and also considering its areal distribution, this pyroclastic flow deposit is considered to be associated with the initial phase of emplacement of the Los Ocotes dome. Indeed, it clearly underlies the Los Ocotes dome but covers all the surrounding domes and cinder cones (i.e., Volcán Tezontle).

CLASSIFICATION AND PETROGRAPHY

The entire San Pedro–Cerro Grande volcanic complex was sampled in detail (Table 1). The overall set of samples was analyzed for major and trace elements (Tables 2 and 3), mineral compositions (Tables 4–9), and rare earth elements (Table 10), and Sr and Nd isotope ratios (Table 11) were determined in selected representative samples.

TABLE 2. ANALYSES OF MAJOR (WT%) AND TRACE ELEMENTS (PPM) OF FIRST PERIOD ROCKS OF THE SAN PEDRO-CERRO GRANDE VOLCANIC COMPLEX

Group	AF	AB	AB	AF	AB	AB	AF	AF	AB	AB	AF	AF	AF	AF	AF	AF	AF	AB	AB	AB	AB	AB	AB	AB	AB
Sample	SPC 146	SPC 124	SPC 132	SPC 117	SPC 56	SPC 55	SPC 139	SPC 118	SPC 125	SPC 130	SPC 131	GC4-74	SPC 116	GC6-288	GC4-118	GC4-170	SPC 129	SPC 108	SPC 123	SPC 122	SPC 126	SPC 127	SPC 19	SPC 58	SPC 57
SiO_2	58.9	61.1	61.8	62.2	62.4	62.7	63.0	63.2	64.1	64.2	64.8	65.0	65.1	65.7	66.2	66.2	66.4	66.9	68.0	68.7	69.0	71.6	72.9	72.9	73.0
TiO_2	0.81	0.61	0.55	0.65	0.57	0.56	0.65	0.65	0.52	0.61	0.66	0.51	0.51	0.54	0.51	0.49	0.35	0.48	0.38	0.35	0.35	0.27	0.13	0.12	0.12
Al_2O_3	16.8	17.6	17.5	16.8	17.0	17.2	16.7	16.6	16.4	16.5	16.0	16.0	16.0	15.4	15.2	15.4	16.5	16.1	15.8	15.1	15.3	14.4	13.2	13.0	12.9
Fe_2O_3	3.41	1.30	1.54	1.67	3.16	1.97	2.68	2.39	1.93	1.88	3.04	4.22	1.41	4.36	4.24	4.15	1.31	3.03	1.58	1.33	1.18	1.12	0.52	0.41	0.41
FeO	2.67	3.50	2.72	3.20	1.24	2.28	2.20	2.60	2.04	2.56	1.64	-	2.46	-	-	-	0.88	0.90	1.56	1.40	1.44	0.60	0.62	0.64	0.64
MnO	0.09	0.09	0.08	0.09	0.08	0.08	0.09	0.09	0.09	0.09	0.07	0.08	0.08	0.06	0.07	0.07	0.07	0.08	0.07	0.07	0.07	0.07	0.07	0.07	0.07
MgO	2.29	2.84	2.89	2.55	2.60	2.49	2.59	2.35	1.82	1.84	1.91	2.13	2.01	2.05	2.14	2.10	0.42	0.84	1.61	1.32	1.32	0.49	0.22	0.20	0.18
CaO	5.47	5.86	5.91	5.48	5.56	5.49	5.55	5.48	4.86	4.95	5.00	4.79	4.67	4.63	4.65	4.71	1.25	3.86	3.65	3.30	3.42	1.92	0.95	0.85	0.85
Na_2O	3.75	3.94	3.64	3.60	3.65	3.46	4.02	4.06	4.14	4.25	4.23	3.88	3.57	4.14	4.19	4.07	2.85	4.53	4.33	4.39	4.33	3.98	3.49	3.75	3.66
K_2O	1.37	1.91	2.05	2.50	2.13	2.15	1.83	1.90	2.32	1.97	2.05	2.48	2.86	2.24	2.17	2.21	3.17	1.91	2.14	2.53	2.45	3.91	3.81	3.96	3.80
P_2O_5	0.15	0.12	0.09	0.13	0.10	0.10	0.14	0.14	0.16	0.15	0.14	0.10	0.10	0.12	0.11	0.10	0.03	0.14	0.09	0.08	0.09	0.06	0.04	0.03	0.03
LOI	4.31	1.16	1.20	1.17	1.49	1.57	0.57	0.56	1.57	1.03	0.49	0.82	1.20	0.84	0.54	0.50	6.79	1.23	0.84	1.45	1.11	1.53	4.02	4.12	4.35
V	107	97	91	107	81	88	111	110	67	80	104	85	82	85	88	87	16	72	62	53	50	17	9	9	9
Cr	9	31	33	29	23	24	30	32	9	3	26	22	16	21	21	18	2	11	12	7	7	bdl	bdl	bdl	bdl
Co	13	13	13	13	14	14	13	16	8	10	12	9	10	12	10	9	bdl	8	7	6	5	bdl	bdl	bdl	bdl
Ni	bdl	bdl	bdl	bdl	10	9	4	bdl	bdl	bdl	bdl	10	bdl	10	8	11	bdl	bdl	bdl	bdl	bdl	bdl	bdl	bdl	bdl
Cu	bdl	bdl	bdl	bdl	bdl	bdl	8	4	bdl	bdl	bdl	bdl	bdl	6	bdl	7	bdl	bdl	bdl	bdl	bdl	bdl	bdl	bdl	bdl
Zn	77	63	55	66	57	57	67	68	60	60	60	59	58	60	58	60	54	51	49	44	40	49	44	42	42
Rb	20	27	27	37	28	28	35	35	31	32	39	45	48	42	42	43	65	32	34	48	48	48	64	62	64
Sr	844	770	780	621	727	732	638	635	674	742	607	523	510	520	518	519	215	725	531	459	457	397	171	153	152
Y	12	7	5	12	5	7	13	16	10	4	14	11	13	12	10	10	24	27	10	9	9	10	9	9	9
Zr	105	114	95	156	111	107	160	162	129	109	156	153	161	170	143	146	203	118	109	112	113	139	116	110	110
Nb	4	3	1	4	3	3	4	5	3	3	4	4	4	5	3	4	13	3	5	5	5	3	6	6	6
Ba	630	735	674	845	816	835	845	898	1029	670	1003	934	969	945	924	918	882	1017	834	849	862	1303	1134	1113	1097
La	16	20	14	21	16	21	22	25	21	15	28	22	25	28	24	26	37	-	22	23	19	23	25	21	23
Ce	32	29	29	46	33	31	48	53	39	34	43	43	48	53	49	48	55	32	39	34	35	43	38	39	46
Nd	20	17	16	24	16	20	23	27	25	18	25	20	23	24	24	23	38	41	18	16	17	21	15	16	19
Pb	11	8	9	11	7	7	9	10	11	7	13	12	13	13	12	12	14	8	9	12	9	14	19	15	15

Note: bdl—below detection limit; - —not determined; AF—amphibole-free group; AB—amphibole-bearing group. Major and trace elements were determined by X-ray fluorescence (XRF) at Dipartimento di Scienze della Terra of the Università degli Studi di Firenze, according to the procedure described by Franzini et al. (1972) for major elements, and that described by Jenkins and De Vries (1971) for trace elements. MgO and Na_2O were determined by atomic absorbtion spectroscopy (AAS), loss on ignition (LOI) by gravimetry, and FeO by titration. The analytical errors for XRF analysis were evaluated to be better than 15% for Pb, better than 10% for Y, La, and Ce, and better than 5% for all other elements.

TABLE 3. ANALYSES OF MAJOR (WT%) AND TRACE ELEMENTS (PPM) OF SECOND PERIOD ROCKS OF THE SAN PEDRO-CERRO GRANDE VOLCANIC COMPLEX

Group	A.N.	A.N.	A.N.	A.N.	A.N.	A.N.	A.N.	A.N.	AF	AF	AF	AB	AB	AB	AB	AB	AB	AB	AB	AB	AB	AB	AB	AB
Sample	SPC 24(1)	SPC 25(1)	SPC 61(1)	SPC 109(1)	SPC 18(1)	SPC 64(1)	SPC 17(1)	SPC 20(1)	SPC 112	SPC 111	SPC 114	SPC 128	SPC 62	SPC 63	SPC 115P	SPC 66	SPC 144	SPC 65	SPC 67	SPC 68	SPC 23	SPC 88	SPC 69	SPC 115F
SiO_2	51.0	52.3	52.3	52.5	53.6	53.6	54.2	54.7	64.3	64.6	64.8	68.1	68.6	69.0	69.3	70.3	70.4	70.4	70.5	70.5	71.7	71.7	72.1	72.5
TiO_2	2.31	1.55	2.22	2.10	2.03	2.04	1.90	1.46	0.59	0.57	0.51	0.38	0.39	0.37	0.22	0.35	0.29	0.34	0.34	0.33	0.29	0.29	0.21	0.17
Al_2O_3	17.7	18.1	16.7	17.0	17.2	17.1	17.1	17.5	16.3	16.2	16.1	15.3	15.0	15.1	15.3	14.9	14.5	14.7	14.7	15.0	14.4	14.2	13.7	13.4
Fe_2O_3	1.80	5.58	1.91	1.32	1.79	1.72	1.50	1.46	1.49	1.54	1.40	1.23	1.28	1.27	0.95	1.74	0.63	2.36	2.48	2.48	0.86	0.96	0.67	0.50
FeO	7.80	2.12	7.72	8.04	7.08	7.08	7.04	6.20	2.96	2.88	2.50	1.72	1.72	1.52	0.64	1.00	1.47	0.32	0.20	0.12	1.20	0.99	0.60	0.72
MnO	0.16	0.14	0.17	0.17	0.16	0.16	0.15	0.14	0.10	0.10	0.08	0.07	0.07	0.07	0.05	0.07	0.06	0.07	0.07	0.07	0.06	0.07	0.05	0.06
MgO	5.17	5.12	4.64	4.67	4.08	3.97	3.93	4.92	1.90	1.82	2.01	1.54	1.53	1.38	0.29	1.24	0.07	1.27	1.33	1.23	0.85	0.81	0.27	0.27
CaO	7.92	7.84	7.44	7.16	7.11	7.09	7.05	6.99	4.47	4.42	4.79	3.80	3.71	3.58	1.13	3.28	2.30	2.91	3.04	2.83	2.44	2.43	1.25	1.18
Na_2O	3.69	3.89	3.75	3.78	3.85	3.78	3.84	4.00	4.19	4.22	3.35	4.16	4.04	4.32	3.17	4.28	4.99	4.26	4.28	4.29	4.43	4.41	3.98	3.69
K_2O	1.62	1.60	1.56	1.71	1.88	1.91	1.92	1.51	2.41	2.32	2.99	2.45	2.50	2.29	3.20	2.39	2.89	2.43	2.46	2.54	2.77	2.87	3.35	3.45
P_2O_5	0.62	0.52	0.61	0.63	0.51	0.58	0.50	0.36	0.18	0.18	0.10	0.08	0.08	0.08	0.03	0.08	0.06	0.08	0.08	0.08	0.07	0.07	0.03	0.03
LOI	0.18	1.21	0.99	0.85	0.76	0.95	0.90	0.71	1.12	1.13	1.44	1.12	1.10	0.98	5.69	0.37	2.37	0.81	0.54	0.51	0.97	1.20	3.81	4.08
V	226	165	211	204	193	192	185	163	75	76	82	61	63	56	15	55	36	42	41	39	36	34	14	13
Cr	48	165	79	75	48	45	53	125	5	9	15	13	10	9	7	5	9	7	6	6	bdl	bdl	bdl	6
Co	35	33	31	25	26	26	25	28	9	9	11	7	7	6	bdl	8	3	6	6	5	bdl	bdl	bdl	bdl
Ni	37	94	40	40	21	22	22	63	bdl	bdl	bdl	bdl	bdl	bdl	bdl	bdl	bdl	bdl	bdl	bdl	bdl	bdl	bdl	bdl
Cu	23	25	23	30	24	21	20	24	bdl	bdl	bdl	bdl	bdl	bdl	bdl	bdl	bdl	bdl	bdl	bdl	bdl	bdl	bdl	bdl
Zn	95	74	106	103	101	99	99	87	72	71	57	46	47	44	35	47	18	44	43	44	41	38	34	32
Rb	15	14	20	21	22	22	22	13	37	35	46	44	44	46	56	46	50	34	42	46	48	51	58	61
Sr	686	597	563	561	559	556	551	604	555	541	515	522	523	494	199	480	352	437	459	424	337	329	236	210
Y	31	30	36	39	35	36	33	26	14	14	13	9	7	8	10	9	14	7	8	8	11	11	8	9
Zr	239	221	256	256	282	280	278	181	160	155	156	107	105	103	140	111	116	107	106	108	113	115	125	119
Nb	25	27	26	24	26	26	24	14	5	5	4	5	5	5	7	6	8	5	5	5	7	7	5	5
Ba	764	643	787	681	734	744	731	731	961	970	984	809	804	841	1069	868	965	937	865	887	972	971	1077	1096
La	30	30	34	36	36	43	34	27	21	27	28	23	17	21	26	19	21	19	22	21	23	22	24	22
Ce	70	50	77	76	66	70	80	49	47	47	42	36	30	36	45	41	35	38	33	35	40	34	39	42
Nd	41	26	46	43	37	38	40	29	25	26	22	20	15	16	17	19	15	17	13	17	16	15	16	17
Pb	9	7	10	12	9	9	11	6	10	14	12	12	9	10	13	11	4	12	11	10	12	13	15	16

Note: bdl—below detection limit; AF—amphibole-free group; AB—amphibole-bearing group; A.N. —Amado Nervo lavas. (1) Samples from Petrone et al. (2003). For analytical technique details see Table 2.

TABLE 4. REPRESENTATIVE MICROPROBE ANALYSES OF PLAGIOCLASE

Sample:	SPC122		SPC 126		SPC 130		SPC 132		SPC 111	
Period:	First		First		First		First		Second	
Group:	Amphibole-bearing		Amphibole-bearing		Amphibole-free		Amphibole-bearing		Amphibole-free	
Texture:	Rim	Rim	Rim	Agg	Core	Agg	Core	Gdm	Core	Agg
(wt%)										
SiO_2	52.3	62.4	60.2	52.3	53.6	46.4	45.9	53.8	61.1	51.3
TiO_2	0.01	0.04	0.03	0.02	0.03	0.02	0.03	0.05	0.02	0.03
Al_2O_3	30.2	23.8	25.2	30.7	29.4	34.2	33.9	29.5	24.4	30.4
Fe_2O_3	0.52	0.22	0.21	0.56	0.46	0.54	0.46	0.62	0.21	0.59
MgO	0.04	bdl	bdl	0.02	0.08	0.05	0.04	0.02	0.05	0.09
CaO	12.91	4.89	6.73	12.51	11.34	16.95	16.97	11.92	5.90	13.36
Na_2O	3.69	7.98	7.40	4.28	4.71	1.47	1.60	4.50	7.63	3.78
K_2O	0.15	0.55	0.44	0.14	0.12	0.02	0.03	0.26	0.59	0.10
SrO	0.18	bdl	0.18	0.09	bdl	0.19	bdl	0.18	0.21	0.21
BaO	0.04	bdl	0.10	bdl	bdl	bdl	bdl	0.02	0.02	0.05
Total	100.0	99.8	100.5	100.6	99.7	99.8	99.0	100.9	100.1	99.8
An %	65.3	24.5	32.5	61.3	56.7	86.3	85.3	58.5	28.9	65.7
Ab %	33.7	72.3	64.8	37.9	42.6	13.6	14.6	40.0	67.6	33.6
Or %	0.9	3.3	2.5	0.8	0.7	0.1	0.2	1.5	3.4	0.6

Sample:	SPC 109		SPC 23		SPC120A/B		SPC 120 A/G		SPC 65	
Period:	Second		Second		Second		Second		Second	
Group:	Mafic		Amphibole-bearing		Amphibole-bearing		Amphibole-bearing		Amphibole-bearing	
Texture:	Gdm	Gdm	Core	Rim	Rim	Agg	Core	Micro	Rim	Micro
(wt%)										
SiO_2	53.9	58.8	55.1	51.8	61.4	48.5	56.0	52.0	60.1	51.5
TiO_2	0.13	0.24	0.05	0.02	0.06	0.06	0.04	0.05	0.02	bdl
Al_2O_3	28.9	24.4	28.0	30.3	25.0	32.5	28.4	30.2	25.4	31.1
Fe_2O_3	0.92	0.91	0.27	0.50	0.19	0.56	0.42	0.51	0.30	0.37
MgO	0.10	0.06	bdl	0.05	bdl	bdl	0.03	0.09	bdl	0.05
CaO	10.82	6.67	9.71	12.92	5.83	14.79	9.43	12.18	6.60	13.20
Na_2O	5.14	6.94	5.56	4.37	7.82	2.95	5.95	4.20	7.34	3.74
K_2O	0.44	1.07	0.25	0.11	0.48	0.10	0.20	0.13	0.40	0.13
SrO	0.13	0.12	0.37	0.24	0.13	0.18	0.26	0.31	0.22	0.40
BaO	0.05	0.05	0.04	bdl	0.07	bdl	0.03	0.02	0.06	0.07
Total	100.5	99.3	99.3	100.4	100.9	99.7	100.7	99.7	100.4	100.6
An %	52.4	32.5	48.3	61.6	28.3	73.0	46.1	61.1	32.4	65.5
Ab %	45.0	61.2	50.1	37.7	67.8	26.4	52.7	38.1	65.2	33.6
Or %	2.5	6.2	1.5	0.6	2.8	0.6	1.2	0.8	2.3	0.8

Note: bdl—values below detection limit; Core—phenocryst core; Rim—phenocryst rim; Micro—micro-phenocryst; Agg—mineral of glomeroporphyritic aggregate; Gdm—mineral in the groundmass. Compositions of major mineral phases were performed at the Dipartimento di Scienze della Terra of the Università degli Studi di Firenze using a JEOL JXA-8600 microprobe operating at 15 kv and 10 nA. Matrix effects were corrected following the Bence and Albee (1968) method. Accuracy and precision estimates are given in Vaggelli et al. (1999). The complete set of analyses is available as item 2006050 in the GSA Data Repository at www.geosociety.org/pubs/ft2006.htm, or on request from editing@geosociety.org or Documents Secretary, GSA, P.O. Box 9140, Boulder, CO 80301, USA.

According to the International Union of the Geological Sciences (IUGS) classification scheme on the total alkalies-silica (TAS) diagram (Le Bas et al., 1992), the San Pedro–Cerro Grande volcanic rocks are bimodal in composition, with hawaiite to mugearite at the mafic end and andesite to rhyolite at the intermediate and felsic end (Fig. 3). In detail, the rocks of the first period range in composition from andesite to rhyolite. Those of the second period are bimodal in composition, with a gap in the range 55–64 wt% of SiO_2 between the dacitic-rhyolitic domes (and associated pyroclastic rocks) and the Amado Nervo hawaiites and mugearites. The Amado Nervo rocks are the only mafic varieties in the San Pedro–Cerro Grande volcanic complex and are transitional Na-alkaline ($Na_2O–2 > K_2O$) in composition. They are quartz-hypersthene and olivine-hypersthene normative. All intermediate and felsic rocks (andesite-dacite-rhyolite) are subalkaline and quartz-hypersthene normative.

Subalkaline rocks (Fig. 3) can be distinguished into two broad groups based on the occurrence of amphibole (Figs. 4 and 5). Amphibole-free rocks have ubiquitous plagioclase and orthopyroxene phenocrysts and microphenocrysts. Clinopyroxene is rare and is almost exclusively found in the groundmass. Amphibole-free andesite (Fig. 4C) is almost aphyric, whereas amphibole-free dacite is porphyritic (10–20 vol% phenocrysts). Resorbed amphibole relics are rarely present, even in the amphi-

TABLE 5. REPRESENTATIVE MICROPROBE ANALYSES OF CLINOPYROXENE AND ORTHOPYROXENE

	Clinopyroxene			Orthopyroxene											
Sample:	SPC 109			SPC 122	SPC 126	SPC 130		SPC 132			SPC 111			SPC 65
Period:	Second			First	First	First		First			Second			Second
Group:	Mafic			Amphibole-bearing	Amphibole-bearing	Amphibole-bearing		Amphibole-bearing			Amphibole-free			Amphibole-bearing
Type:	Gdm	Gdm	Gdm	Micro	Gdm	Gdm	Core	Gdm	Rim	Agg	Core	Rim	Gdm	Micro
(wt%)														
SiO_2	46.6	47.7	48.4	53.1	54.7	52.4	53.7	52.3	54.4	56.0	53.3	51.4	52.4	53.2
TiO_2	3.35	2.40	2.53	0.20	0.11	0.34	0.31	0.34	0.25	0.11	0.33	0.32	0.29	0.20
Al_2O_3	3.66	3.52	3.13	1.49	1.27	2.79	1.22	3.00	2.17	0.98	2.56	3.87	3.23	2.06
Cr_2O_3	bdl	0.08	0.01	bdl	0.02	bdl	0.05	0.10	0.18	0.13	0.16	0.01	bdl	0.05
Fe_2O_3	3.71	3.96	1.33	1.91	1.82	2.96	1.46	2.77	2.31	0.56	1.50	2.75	2.38	1.87
FeO	8.58	8.36	10.56	16.40	14.97	14.12	16.03	12.46	10.19	11.88	14.01	14.91	15.20	15.79
MnO	0.31	0.23	0.27	0.88	0.6	0.49	0.46	0.40	0.26	0.23	0.29	0.46	0.47	0.54
MgO	11.5	12.5	12.4	25.4	27.3	26.2	25.6	26.9	29.7	29.7	26.5	24.6	25.2	25.6
CaO	20.7	20.1	20.1	0.85	0.92	1.37	1.68	1.48	1.16	1.33	1.88	1.60	1.55	1.23
Na_2O	0.57	0.54	0.32	0.03	bdl	bdl	0.06	bdl	0.09	0.04	bdl	0.09	0.06	0.05
Total	99.1	99.4	99.1	100.2	101.8	100.7	100.6	99.8	100.6	101.0	100.5	100.0	100.7	100.6
Mg#	0.63	0.61	0.65	0.70	0.70	0.73	0.72	0.76	0.81	0.81	0.75	0.71	0.72	0.72

Note: bdl—values below detection limit; Core—phenocryst core; Rim—phenocryst rim; Micro—micro-phenocryst; Agg—mineral of glomeroporphyritic aggregate; Gdm—mineral in the groundmass. Compositions of major mineral phases were performed at the Dipartimento di Scienze della Terra of the Università degli Studi di Firenze using a JEOL JXA-8600 microprobe operating at 15 kv and 10 nA. Matrix effects were corrected following the Bence and Albee (1968) method. Accuracy and precision estimates are given in Vaggelli et al. (1999). The complete set of analyses is available as item 2006050 in the GSA Data Repository at www.geosociety.org/pubs/ft2006.htm, or on request from editing@geosociety.org or Documents Secretary, GSA, P.O. Box 9140, Boulder, CO 80301, USA.

bole-free group. Amphibole-bearing rocks range in composition from andesite to rhyolite, and are characterized by seriate porphyritic textures (~20% phenocryst; Fig. 4A–B) with intersertal-intergranular groundmass, which can be hyaline in rhyolites (Fig. 4D). Plagioclase, amphibole, and orthopyroxene are ubiquitous; clinopyroxene is rare and restricted to the groundmass. Few quartz crystals are found in dacites and rhyolites. Both amphibole-free and amphibole-bearing rocks have similar minor and accessory phases; opaque minerals are abundant as microphenocrysts, biotite is present as pheno- and microphenocrysts in the dacitic and rhyolitic rocks, and apatite constitutes a common accessory phase restricted to the groundmass along with opaque minerals.

Amado Nervo lavas show seriate subporphyritic textures with intersertal groundmass (Fig. 4E), with olivine (>5 vol%) being the only phenocryst in a groundmass of plagioclase, olivine, opaques, and clinopyroxene.

In summary, on the basis of petrographic analysis, a threefold subdivision can be established among rocks of the San Pedro–Cerro Grande volcanic complex: Amado Nervo mafic rocks, amphibole-free, and amphibole-bearing intermediate to felsic rocks. The estimated volume of Amado Nervo volcano (8.62 km³) is comparable to minimum volume estimates of amphibole-bearing rocks (8.58 km³) calculated on the basis of volumes given by Frey et al. (2004a). It is worth noting that

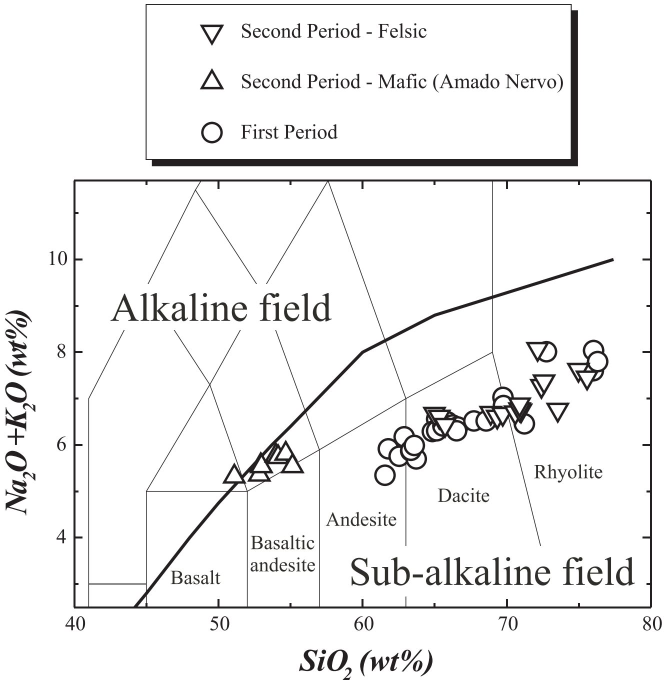

Figure 3. Total alkali-silica classification diagram (Le Bas et al., 1992) (water-free basis) of the San Pedro–Cerro Grande volcanic complex rocks. The Irvine and Baragar (1971) line (heavy line) is also reported.

TABLE 6. REPRESENTATIVE MICROPROBE ANALYSES OF AMPHIBOLE

Sample:	SPC 122		SPC 126		SPC 130		SPC 132		SPC 111		SPC 120A/B		SPC23		SPC 65	
Period:	First		First		First		First		Second		Second		Second		Second	
Group:	Amphibole-bearing		Amphibole-bearing		Amphibole-bearing		Amphibole-bearing		Amphibole-free		Amphibole-bearing		Amphibole-bearing		Amphibole-bearing	
Texture:	Core	Rim	Core	Rim	Core	Agg	Core	Agg	Core	Micro	Agg	Agg	Agg	Micro	Core	Agg
(wt%)																
SiO_2	42.9	49.5	42.9	44.5	43.8	43.0	42.5	44.2	40.1	49.0	42.5	45.7	44.1	48.9	43.2	44.6
TiO_2	3.03	0.94	1.88	1.84	2.28	2.47	3.03	2.53	3.81	1.54	1.86	1.65	1.80	0.98	2.92	1.44
Al_2O_3	11.5	5.9	12.4	11.6	10.6	11.8	11.0	11.0	14.1	11.7	12.4	9.2	12.1	6.2	10.8	12.4
Cr_2O_3	bdl	0.01	bdl	0.06	bdl	0.04	bdl	0.29	bdl	0.01	bdl	bdl	0.10	0.01	0.03	bdl
Fe_2O_3	bdl	0.99	0.96	1.18	1.21	0.71	3.52	0.28	2.51	bdl	1.19	2.09	1.25	0.93	bdl	1.31
FeO	12.8	11.8	9.65	8.94	11.6	8.54	14.3	10.0	11.2	5.96	11.3	10.6	8.21	11.2	12.0	8.20
MnO	0.27	0.86	0.12	0.14	0.33	0.09	0.24	0.11	0.33	0.20	0.16	0.34	0.13	0.77	0.22	0.15
MgO	13.7	15.7	15.1	16.0	14.8	15.9	10.2	15.7	13.9	11.8	13.9	15.5	16.3	16.2	14.7	16.4
CaO	11.2	11.1	11.2	11.1	10.5	11.3	13.4	11.1	10.0	18.2	10.6	10.9	11.4	10.6	11.0	10.9
Na_2O	2.49	1.09	2.38	2.09	2.13	2.40	1.73	2.13	2.35	1.01	2.08	1.76	2.33	1.29	2.42	2.12
K_2O	0.56	0.33	0.39	0.29	0.43	0.27	0.24	0.40	0.37	0.12	0.39	0.40	0.38	0.26	0.47	0.30
F	bdl	0.11	0.19	0.14	bdl	bdl	bdl	bdl	0.27	0.13	bdl	0.13	0.21	0.12	bdl	bdl
Cl	bdl	0.03	0.02	bdl	bdl	bdl	bdl	0.02	0.02	0.02	0.02	0.03	bdl	0.03	bdl	bdl
Total	98.52	98.37	97.14	97.85	97.73	96.47	100.01	97.73	98.98	99.69	96.42	98.29	98.23	97.64	97.69	97.80
F+Cl=O	-	0.05	0.08	0.06	-	-	-	0.02	0.12	0.06	-	0.06	0.09	0.06	-	-
Total	98.52	98.32	97.05	97.79	97.73	96.47	100.01	97.72	98.86	99.63	96.41	98.23	98.14	97.59	97.69	97.80
Mg#	0.65	0.67	0.72	0.74	0.67	0.75	0.51	0.73	0.64	0.77	0.66	0.68	0.75	0.69	0.68	0.75

Note: bdl—values below detection limit; Core—phenocryst core; Rim—phenocryst rim; Micro—micro-phenocryst; Agg—mineral of glomeroporphyritic aggregate. Compositions of major mineral phases were performed at the Dipartimento di Scienze della Terra of the Università degli Studi di Firenze using a JEOL JXA-8600 microprobe operating at 15 kv and 10 nA. Matrix effects were corrected following the Bence and Albee (1968) method. Accuracy and precision estimates are given in Vaggelli et al. (1999). The complete set of analyses is available as item 2006050 in the GSA Data Repository at www.geosociety.org/pubs/ft2006.htm, or on request from editing@geosociety.org or Documents Secretary, GSA, P.O. Box 9140, Boulder, CO 80301, USA.

TABLE 7. REPRESENTATIVE MICROPROBE ANALYSES OF MICA

Sample:	SPC 122		SPC 126		SPC 111		SPC 120A/B		SPC23		SPC 65	
Period:	First		First		Second		Second		Second		Second	
Group:	Amphibole-bearing		Amphibole-bearing		Amphibole-free		Amphibole-bearing		Amphibole-bearing		Amphibole-bearing	
Type:	Core	Rim	Core	Agg	Agg	Rim	Agg	Core	Rim	Micro	Core	Rim
(wt%)												
SiO_2	38.1	37.7	38.2	37.4	36.4	36.9	37.6	38.28	36.7	37.9	36.3	36.0
TiO_2	4.18	3.87	4.17	4.18	3.79	3.79	3.93	4.09	4.05	4.11	4.23	4.10
Al_2O_3	14.1	13.8	14.2	14.5	14.0	14.1	14.8	14.6	13.9	14.0	14.8	15.0
Cr_2O_3	0.02	bdl	0.02	0.03	bdl	bdl	bdl	0.03	bdl	0.03	bdl	bdl
FeO	13.3	12.8	13.5	13.8	17.4	17.9	13.8	13.4	13.8	13.5	16.3	15.9
MnO	0.14	0.21	0.23	0.19	0.35	0.44	0.20	0.23	0.22	0.22	0.30	0.20
MgO	16.1	16.1	15.9	16.1	13.5	13.3	15.7	16.7	15.9	16.0	14.8	15.2
CaO	0.01	0.02	0.26	bdl	0.03	0.03	bdl	0.07	bdl	0.03	0.03	0.01
Na_2O	0.94	0.92	0.65	0.93	0.67	0.69	0.74	0.81	1.08	0.83	0.69	0.96
K_2O	8.16	7.82	7.39	8.45	9.10	8.74	8.17	7.77	8.29	8.66	7.90	8.38
BaO	bdl	0.72	0.67	1.07	0.77	0.88	0.83	0.69	0.64	0.77	0.84	0.87
F	bdl	0.36	0.31	0.28	0.09	0.33	0.24	bdl	0.13	0.18	0.42	1.67
Cl	bdl	0.04	0.05	0.06	0.03	0.03	0.05	0.07	0.05	0.06	0.08	0.06
Total	99.05	98.17	99.64	100.88	101.01	100.89	100.00	100.93	98.66	100.23	100.47	101.45
F+Cl=O	0.00	0.16	0.14	0.13	0.04	0.15	0.11	0.02	0.07	0.09	0.19	0.72
Total	99.05	98.01	99.46	100.75	99.97	100.75	99.89	100.91	98.59	100.14	100.28	100.74
Mg#	0.68	0.69	0.67	0.67	0.58	0.56	0.67	0.69	0.67	0.67	0.61	0.63

Note: bdl—values below detection limit; Core—phenocryst core; Rim—phenocryst rim; Micro—micro-phenocryst; Agg—mineral of glomeroporphyritic aggregate. Compositions of major mineral phases were performed at the Dipartimento di Scienze della Terra of the Università degli Studi di Firenze using a JEOL JXA-8600 microprobe operating at 15 kv and 10 nA. Matrix effects were corrected following the Bence and Albee (1968) method. Accuracy and precision estimates are given in Vaggelli et al. (1999). The complete set of analyses is available as item 2006050 in the GSA Data Repository at www.geosociety.org/pubs/ft2006.htm, or on request from editing@geosociety.org or Documents Secretary, GSA, P.O. Box 9140, Boulder, CO 80301, USA.

TABLE 8. REPRESENTATIVE MICROPROBE ANALYSES OF OXIDES

Sample	SPC 122		SPC 126		SPC 130		SPC 132		SPC 111		SPC 109		SPC 23		SPC 65	
Period	First		First		First		First		Second		Second		Second		Second	
Group	Amphibole-bearing		Amphibole-bearing		Amphibole-bearing		Amphibole-bearing		Amphibole-free		Mafic		Amphibole-bearing		Amphibole-bearing	
Texture	Core	Core	Core	Agg	Core	Gdm	Agg	Micro	Micro	Gdm	Micro	Gdm	Core	Agg	Core	Micro
(wt%)																
SiO_2	0.04	bdl	bdl	0.18	0.06	0.24	bdl	bdl	0.17	0.15	0.02	0.11	0.89	0.05	bdl	0.06
TiO_2	8.01	36.81	5.27	5.12	7.68	13.4	8.33	2.78	7.16	14.90	11.6	21.4	0.01	14.1	0.88	2.8
Al_2O_3	2.47	0.39	2.37	1.95	3.19	1.41	3.16	7.64	1.75	1.31	7.89	1.46	0.33	1.23	2.68	6.54
Cr_2O_3	0.11	bdl	0.03	0.06	bdl	bdl	0.05	0.07	bdl	bdl	16.6	0.59	bdl	bdl	bdl	0.03
Fe_2O_3	50.2	31.2	56.3	56.6	52.0	41.5	50.5	58.1	53.9	38.9	22.4	25.1	64.3	39.6	65.6	56.4
FeO	36.0	29.3	34.2	34.0	36.2	39.7	36.6	25.2	36.1	42.1	36.3	47.6	30.4	40.7	28.4	31.8
MnO	0.47	0.43	0.58	0.65	0.40	0.55	0.31	0.36	0.44	0.65	0.36	0.59	0.27	0.49	1.20	0.57
MgO	1.28	1.88	0.95	1.02	1.64	1.63	1.68	6.12	1.24	1.58	4.29	1.76	0.29	1.64	1.91	1.56
CaO	0.06	0.03	bdl	bdl	0.07	0.88	0.04	0.10	0.04	0.02	bdl	0.04	0.09	0.02	0.02	0.03
Total	98.7	100.1	99.7	99.7	101.2	99.2	100.6	100.4	100.8	99.5	99.4	98.7	96.6	97.9	100.7	99.8
Usp	23.6	-	14.9	14.4	22.3	38.7	24.4	8.1	20.4	42.8	50.3	62.6	0.0	41.1	0.6	8.1
Mt	76.4	-	85.1	85.6	77.7	61.3	75.6	91.9	79.6	57.2	49.7	37.4	100.4	58.9	99.4	91.9
Ilm		67.8														
Hem		32.2														
Cr#											0.6					

Note: Ulvospinel (Usp) end-member is calculated following the scheme of Spencer and Lindsley (1981); Mt—magnetite; Ilm—ilmenite; Hem—hematite; Cr# = [Cr/(Cr+Al)]. bdl—values below detection limit; Core—phenocryst core; Micro—micro-phenocryst; Agg—mineral of glomeroporphyritic aggregate; Gdm—mineral in the groundmass. Compositions of major mineral phases were performed at the Dipartimento di Scienze della Terra of the Università degli Studi di Firenze using a JEOL JXA-8600 microprobe operating at 15 kv and 10 nA. Matrix effects were corrected following the Bence and Albee (1968) method. Accuracy and precision estimates are given in Vaggelli et al. (1999). The complete set of analyses is available as item 2006050 in the GSA Data Repository at www.geosociety.org/pubs/ft2006.htm, or on request from editing@geosociety.org or Documents Secretary, GSA, P.O. Box 9140, Boulder, CO 80301, USA.

TABLE 9. REPRESENTATIVE MICROPROBE ANALYSES OF OLIVINE

Sample:	SPC 109			
Period:	Second			
Group:	Mafic			
Type:	Core	Rim	Gdm	Agg
(wt%)				
SiO_2	38.4	37.8	34.3	39.5
TiO_2	0.03	bdl	0.16	bdl
Al_2O_3	bdl	0.04	2.09	bdl
Cr_2O_3	bdl	bdl	bdl	bdl
Fe_2O_3	1.78	2.05	0.00	0.78
FeO	20.5	21.7	37.4	20.3
MnO	0.36	0.44	0.77	0.34
NiO	0.17	0.15	0.07	0.13
MgO	40.1	38.6	25.0	41.4
CaO	0.19	0.21	0.39	0.14
Total	101.5	101.0	100.2	102.7
Fo (%)	75.9	73.9	53.6	77.4

Note: bdl—values below detection limit; Core—phenocryst core; Rim—phenocryst rim; Agg—mineral of glomeroporphyritic aggregate; Gdm—mineral in the groundmass. Compositions of major mineral phases were performed at the Dipartimento di Scienze della Terra of the Università degli Studi di Firenze using a JEOL JXA-8600 microprobe operating at 15 kv and 10 nA. Matrix effects were corrected following the Bence and Albee (1968) method. Accuracy and precision estimates are given in Vaggelli et al. (1999). The complete set of analyses is available as item 2006050 in the GSA Data Repository at www.geosociety.org/pubs/ft2006.htm, or on request from editing@geosociety.org or Documents Secretary, GSA, P.O. Box 9140, Boulder, CO 80301, USA.

amphibole-free and amphibole-bearing rocks are contemporaneous but spatially separated. Indeed, the amphibole-free rocks from the Atarjea de Tescalame, Corral Falso, Los Ixletes domes, and GC4 well are geographically restricted to an area southeast of the San Pedro domes (Fig. 5).

Magmatic Inclusions

Rounded magmatic inclusions are found hosted in amphibole-bearing rocks, whereas they are rarely hosted in amphibole-free rocks. They are less than 0.5 cm in diameter, but some larger (up to 10 cm) inclusions are also found. The most common enclaves are characterized by variably porphyritic textures (Fig. 4F) with plagioclase, amphibole, and minor clinopyroxene and opaque minerals as phenocrysts. Rarely, accessory zircon is found. Aphyric inclusions with diktytaxitic textures (Fig. 4G) and variable amounts of plagioclase, amphibole, clinopyroxene, opaque, and orthopyroxene microlites are subordinately found. Few mafic cumulate inclusions are also found in the Amado Nervo rocks; these contain olivine, plagioclase, and subordinately clinopyroxene phenocrysts set in a microcrystalline intercumulus matrix.

MINERAL COMPOSITIONS

Plagioclase is euhedral to subhedral and commonly contains glass or groundmass inclusions. Phenocrysts in felsic rocks range in composition from An_{25} to An_{88} (Table 4, Fig. 6). Phenocrysts

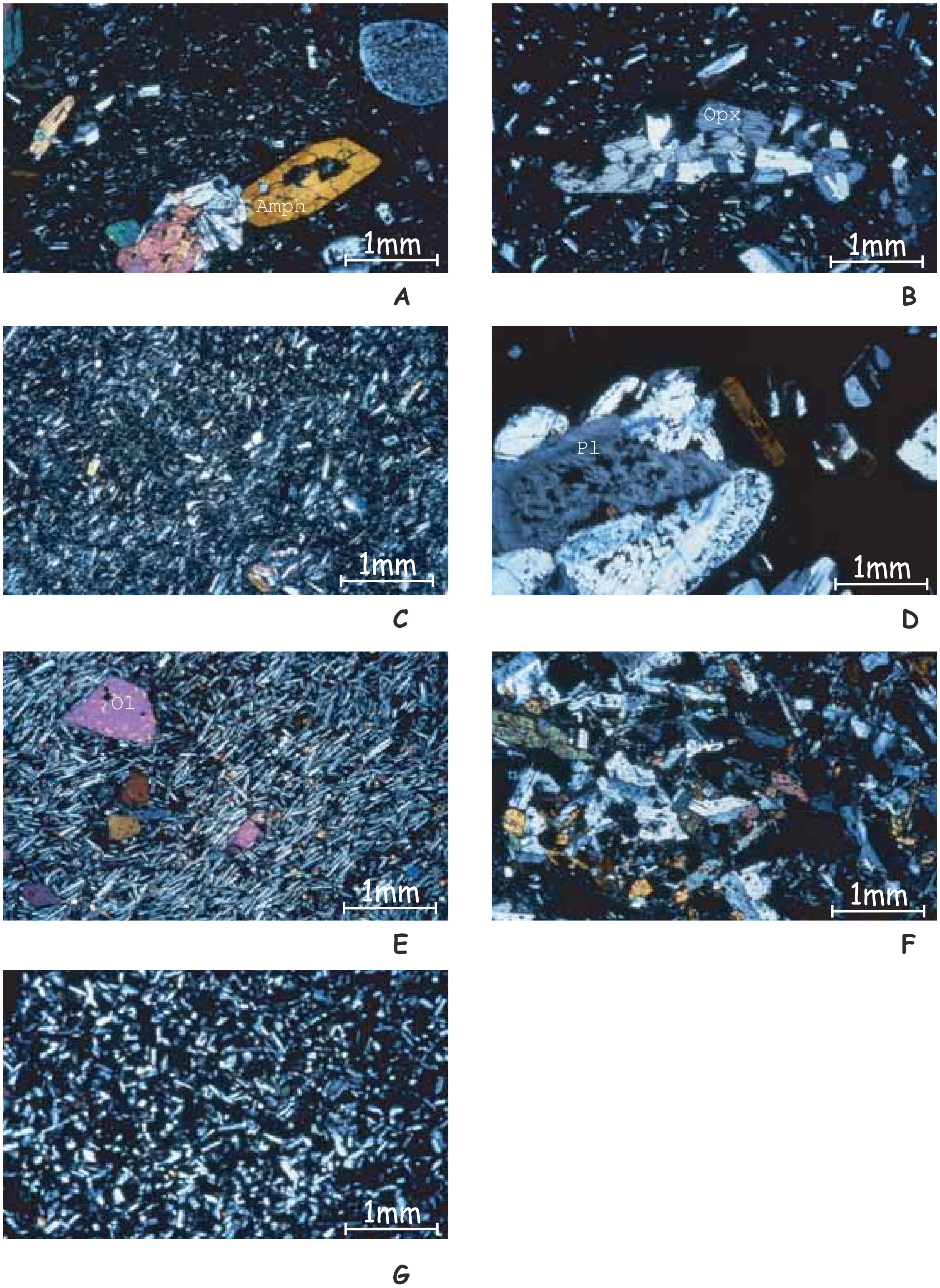

Figure 4. Photomicrographs of different textures shown by San Pedro–Cerro Grande volcanic complex rocks: (A) and (B) first-period amphibole-bearing porphyritic rock (SPC125 and SPC124); (C) first-period amphibole-free aphyric rock (SPC117); (D) vitrophyric texture in a second-period amphibole-bearing rock (SPC23); (E) subporphyritic texture with olivine phenocrysts in the second-period mafic Amado Nervo rock (SPC109); (F) porphyritic texture in a magmatic enclave hosted in a first-period amphibole-bearing rock (SPC130); and (G) diktytaxitic texture of an aphyric magmatic enclave hosted in a first-period amphibole-bearing rock (SPC123). Amph—amphibole, Opx—orthopyroxene, Pl—plagioclase, Ol—olivine.

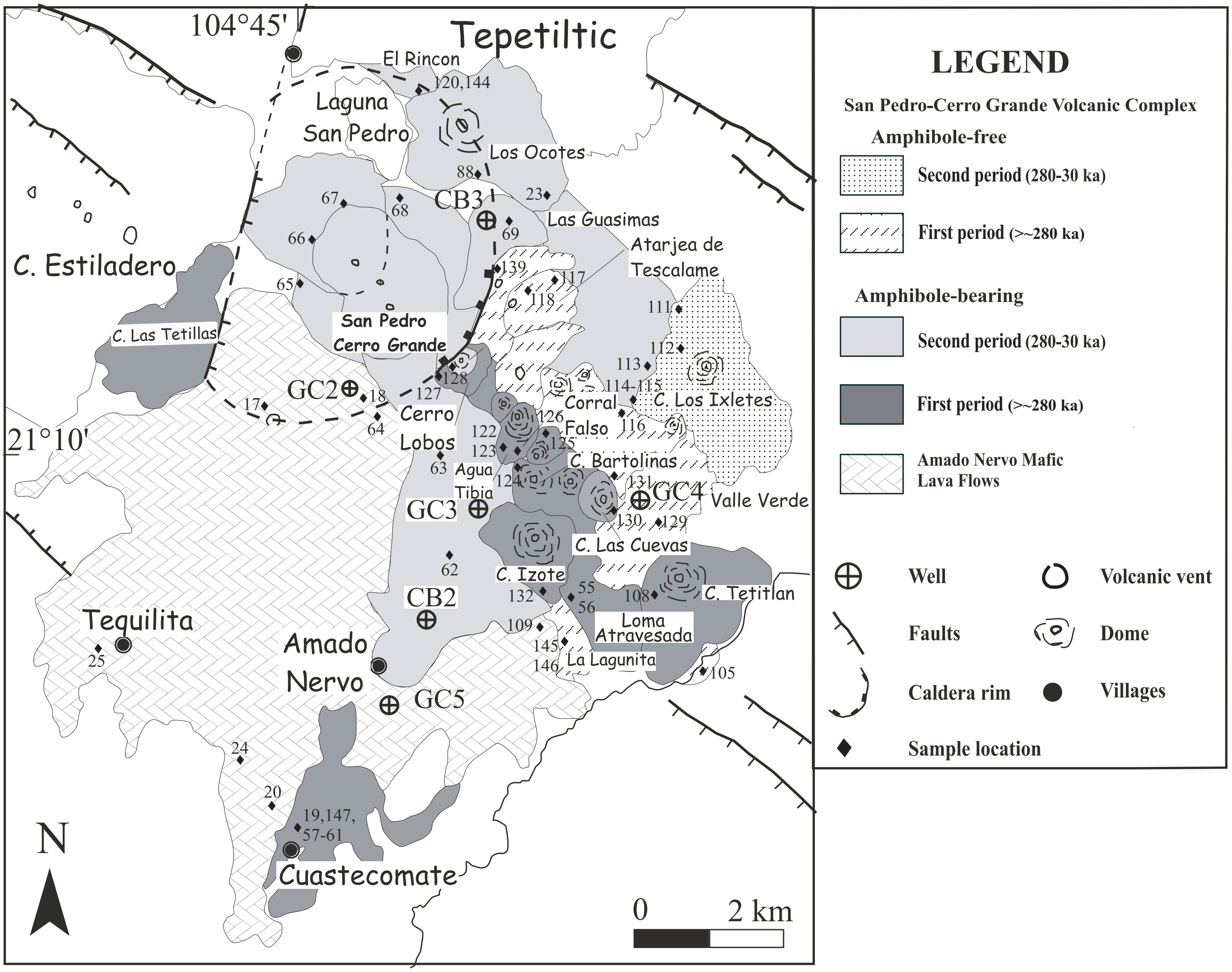

Figure 5. Schematic map showing the areal distribution of amphibole-free and amphibole-bearing rocks in the San Pedro–Cerro Grande volcanic complex. Sampling localities are also shown.

from first-period amphibole-bearing rocks show the highest variation, with andesite to low-silica dacite having the most anorthitic plagioclase (An_{53-88}), and are also characterized by the strongest normal, inverse, and oscillatory zoning (Fig. 6). Groundmass plagioclase is more albitic. Phenocrysts from first-period amphibole-bearing high-silica dacites (SPC122, SPC126) show the largest compositional range (An_{25}–An_{73}) and are prevalently normally zoned. Groundmass plagioclase has intermediate compositions. Plagioclase in second-period rocks is characterized by intermediate compositions (An_{31-67}). Crystals from the Las Guásimas pyroclastic rocks (SPC120) have a wide compositional range (An_{25-78}), with a compositional gap between An_{30} and An_{48}. Plagioclase from Amado Nervo lavas (SPC109) is characterized by almost homogeneous intermediate compositions (An_{49-52}).

Orthopyroxene is present as euhedral phenocrysts and microphenocrysts. It is ubiquitous in andesitic to rhyolitic samples and ranges in composition from bronzite to hypersthene (Table 5), from En_{79} to En_{65} (Fig. 7). There are no differences in orthopyroxene compositions among intermediate to felsic rocks of the two different periods, or between amphibole-free and amphibole-bearing rocks. Normal or reverse zoning is rarely present.

Clinopyroxene is very rare in intermediate to felsic rocks and, when present, is restricted to the groundmass. No analyses are available because of its small crystal size. On the other hand, clinopyroxene from the Amado Nervo lavas is Ti-rich augite to diopside (Table 5, Fig. 7).

Amphibole is euhedral to subhedral with frequent opacite rims, especially in first-period rocks. Amphiboles span a large

TABLE 10. TRACE ELEMENTS ANALYZED BY INSTRUMENTAL NEUTRON ACTIVATION ANALYSIS FOR SELECTED SAN PEDRO–CERRO GRANDE VOLCANIC COMPLEX SAMPLES.

Composition:	SPC 55	SPC 123	SPC 124	SPC 130	SPC 132	SPC 66	SPC 24	SPC 25	SPC 18
Sample:	First	First	First	First	First	Second	Second	Second	Second
La	22.2	22.0	16.8	16.5	14.3	19.3	31.3	28.5	38.4
Ce	32.3	34.3	30.7	30.4	25.4	35.9	70.1	58	80
Nd	19	13	16	14	11	15	31	25	34
Sm	3.9	3.8	3.3	3.3	3.0	3.2	7.72	6.7	8.45
Eu	1.05	0.79	1.04	0.96	0.87	0.77	2.51	1.85	2.49
Tb	0.41	0.34	0.67	0.45	0.32	0.47	1.09	1.08	0.95
Yb	1.5	1.5	1.4	1.3	1.2	1.5	3.1	3.1	3.1
Lu	0.25	0.25	0.24	0.22	0.23	0.29	0.46	0.51	0.54
Th	2.11	3.84	1.95	2.72	2.03	4.34	2.4	2.5	2.9
Ta	0.36	0.7	0.4	0.56	0.35	0.86	2.06	2.3	1.9
Hf	2.8	2.9	2.9	2.8	2.5	3.1	5.4	4.7	6.0
Sc	10.0	7.5	10.6	7.1	10.5	6.8	23.8	21.9	20.5
Co	13.0	9.0	14.3	10.0	13.7	7.5	34.0	29.3	25.1
La_N/Sm_N	3.7	3.8	3.3	3.2	3.1	3.9	2.6	2.7	2.9
Tb_N/Yb_N	1.2	1.1	2.2	1.6	1.2	1.4	1.6	1.6	1.4
Eu/Eu*	1.1	1.0	0.9	1.0	1.2	0.8	1.1	0.9	1.2

Note: Data for SPC24, SPC25 and SPC18 samples are from Petrone et al. (2003). N: values normalized to primitive mantle from Sun and McDonough (1989). Rare earth elements, Th, Hf, Ta, Co, and Sc contents were determined by instrumental neutron activation analyses (INAA) at the Dipartimento di Scienze della Terra of the Università degli Studi di Firenze, following the method described by Poli et al. (1977). The errors for INAA were evaluated to be better than 15% for Tb and Lu, better than 10% for Nd, and Yb, and better than 5% for all other elements.

TABLE 11. Sr AND Nd ISOTOPIC DATA FOR SELECTED ROCKS FROM THE SAN PEDRO–CERRO GRANDE VOLCANIC COMPLEX

Sample:	SPC 117[‡]	SPC 123[†]	SPC 124[†]	SPC 131[‡]	SPC 130[‡]	SPC 132[†]	SPC 66[†]	SPC 24[§]	SPC 25[§]	SPC 109[§]	SPC 64[§]
Period:	First	First	First	First	First	First	Second	Second	Second	Second	Second
$^{87}Sr/^{86}Sr$	0.704110	0.703821	0.704007	0.704243	0.703827	0.703941	0.703848	0.703804	0.703509	0.703872	0.703884
2SE	8	10	9	9	10	10	11	9	16	12	16
$^{143}Nd/^{144}Nd$	n.d.	0.512785	0.512789	n.d.	n.d.	0.512794	0.512712	0.512893	0.512946	0.512877	0.512883
2SE	n.d.	21	7	n.d.	n.d.	6	15	12	8	6	6
ε_{Nd}	n.d.	2.87	2.94	n.d.	n.d.	3.04	1.44	5.46	5.66	4.31	4.43

Note: n.d.—not determined; Sr and Nd isotope ratios were determined at:

[†] Laboratorio Universitario de Geoquímica Isotópica (LUGIS), Instituto de Geofísica of the Universidad Nacional Autónoma de México (UNAM) using a Finnigan MAT 262 multi-collector mass spectrometer.

[‡] Dipartimento Scienze della Terra, Università degli Studi di Firenze using a Thermofinnigan Triton®-TI mass spectrometer equipped with nine Faraday cups in a static rotative mode. Analytical procedures for analyses performed at UNAM are given in Schaaf et al. (2000). All errors reported are 2SE (2 standard error of the mean) for within-run precisions and 1SD (1 standard deviation) for standards. All Sr data are corrected for mass fractionation to $^{86}Sr/^{88}Sr = 0.1194$ and normalized to a value of $^{87}Sr/^{86}Sr = 0.71025$ for NBS987 standard. $^{87}Sr/^{86}Sr$ values for NBS987 measured at LUGIS during the course of these analyses was 0.710234 ± 16 (*n* =135) compared to the reported value of 0.71025. Isotopic ratios of Nd were corrected for fractionation to $^{146}Nd/^{144}Nd = 0.7129$ and normalized to a value of $^{143}Nd/^{144}Nd = 0.511860$ for the La Jolla standard. $^{143}Nd/^{144}Nd$ values for La Jolla standard, measured at LUGIS, over the course of this work yielded 0.511879 ± 22 (*n* = 51). Procedure for isotopic analyses performed at the Università degli Studi di Firenze are given in Avanzinelli et al. (2001). All errors reported are 2SE for within-run precision and 2SD for standards. All Sr data are corrected for mass fractionation to $^{86}Sr/^{88}Sr = 0.1194$ and reported relative to a value of $^{87}Sr/^{86}Sr = 0.71025$ for NBS987 standard. $^{87}Sr/^{86}Sr$ values for NBS987 standard measured in Firenze during the course of this work yielded 0.710268 ± 16 (*n* = 30). Bias between measurements performed with the two different mass spectrometers was within the analytical error.

[§] Isotope data for samples SPC24, SPC25, SPC109, and SPC64 are from Petrone et al. (2003). Values are normalized to the accepted values for the standards as reported in Petrone et al. (2003). Analytical details for these samples are reported in Petrone et al. (2003).

compositional range and can be divided, following the scheme of Leake et al. (1997), into low-Al (6–8 wt% Al_2O_3) Mg-hornblende, high-Al (8–14 wt% Al_2O_3) pargasite and edenite, and very high-Al (14–15 wt% Al_2O_3) gedrite populations (Table 6). Most amphiboles fall in the pargasite-edenite field having Al_2O_3 in the range 9–13 wt%. The largest range in composition (Mg-hornblende–pargasite–gedrite) is shown by amphiboles of a first-period high-silica dacite (SPC122) and a second-period rhyolite (SPC23), in contrast to the almost uniform compositions of amphibole (pargasite-edenite) shown by amphiboles of other analyzed first- and second-period rocks.

Mica is prevalently found in the most silica-rich rocks. It is euhedral to subhedral, and ranges in composition from phlogopite to biotite (Table 7). Phlogopite is present only in more evolved first-period amphibole-bearing rocks. Phlogopite and biotite are both present in second-period felsic rocks, with the former more frequent. In sample SPC23 from the Los Ocotes dome on the caldera rim (Fig. 5), only phlogopite is found, but with a relatively

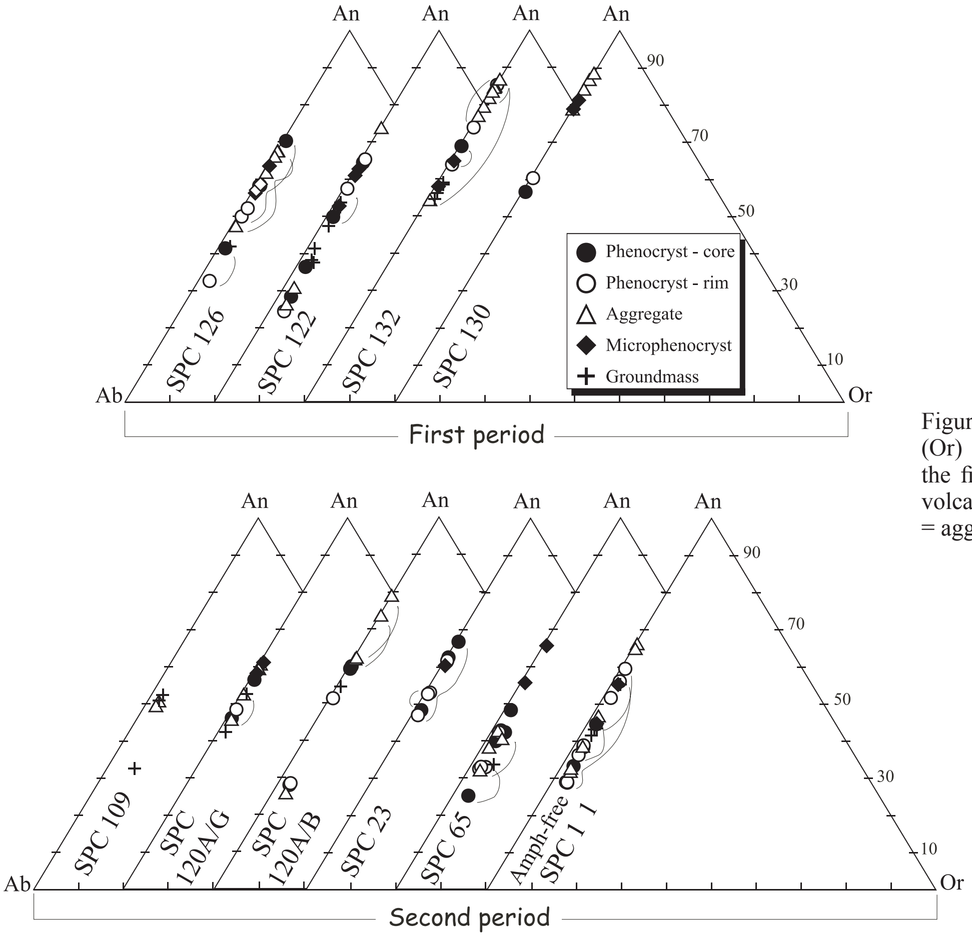

Figure 6. Anorthite (An)–albite (Ab)–orthoclase (Or) classification diagrams for plagioclase of the first and second San Pedro–Cerro Grande volcanic complex periods. Symbols: aggregate = aggregate of crystals.

low Mg/Fe ratio that is close to the boundary with biotite compositions. On the other hand, the only mica present in a amphibole-free second-period rock sample (SPC111) is biotite, which is also characterized by the lowest Mg/Fe ratio and Mg#, and the highest Ba and Mn contents.

Magnetite is the most common Fe-Ti oxide mineral present in the San Pedro–Cerro Grande volcanic complex. It has ulvöspinel (USP) contents that vary between 0.6 and 76 mol% (Table 8). Ti-magnetite compositions (USP_{13} –USP_{76}) are found in all rocks; magnetite is restricted to Los Ocotes and San Pedro–Cerro Grande domes of the second period. The presence of this Ti-poor composition clearly results from subsolidus exsolution (Bacon and Hirschmann, 1988; Frost and Lindsley, 1991). Ilmenite is found limited to second-period rocks of the San Pedro–Cerro Grande domes (samples SPC65 and SPC68), and to sample SPC122 belonging to the amphibole-bearing rocks of the first period of activity. Cr-rich spinel (Cr# = 0.58) is found enclosed in olivine phenocrysts and in the groundmass of olivine-bearing rocks of the Amado Nervo lavas (Tables 8).

Olivine is found only in Amado Nervo lavas with euhedral to subhedral habitus sometimes showing iddingsite rims. It ranges in composition from Fo_{53} to Fo_{78} (Table 9), with groundmass crystals being more fayalitic than phenocrysts.

Mineral compositions of seven magmatic inclusions were analyzed in order to characterize them with respect to their host rocks. No differences are observed between chemical compositions of mineral phases (plagioclase, pyroxene, amphibole, and opaque minerals) in magmatic inclusions and minerals in the host rocks. Compositional variability of mineral phases in inclusions spans a narrow range (i.e., olivine of inclusions hosted by Amado Nervo lavas). In other cases (i.e., plagioclase in inclusions hosted by the Amado Nervo lavas), less evolved compositions are observed.

PRE-ERUPTIVE MAGMA CONDITIONS

The Al-in-hornblende geobarometer (Johnson and Rutherford, 1989) was applied to samples of the amphibole-bearing group; in particular to sample SPC122 from the first-period sequence and to sample SPC65 from rocks of the second period. The application of this geobarometer is justified by the presence of all required phases. Both rocks also contain small amounts of quartz, but lack alkali feldspar, which was not found critical for the geobarometer (Johnson and Rutherford, 1989; Venezky and Rutherford, 1999). Chemical compositions of rims from large amphibole phenocrysts were used for applying the

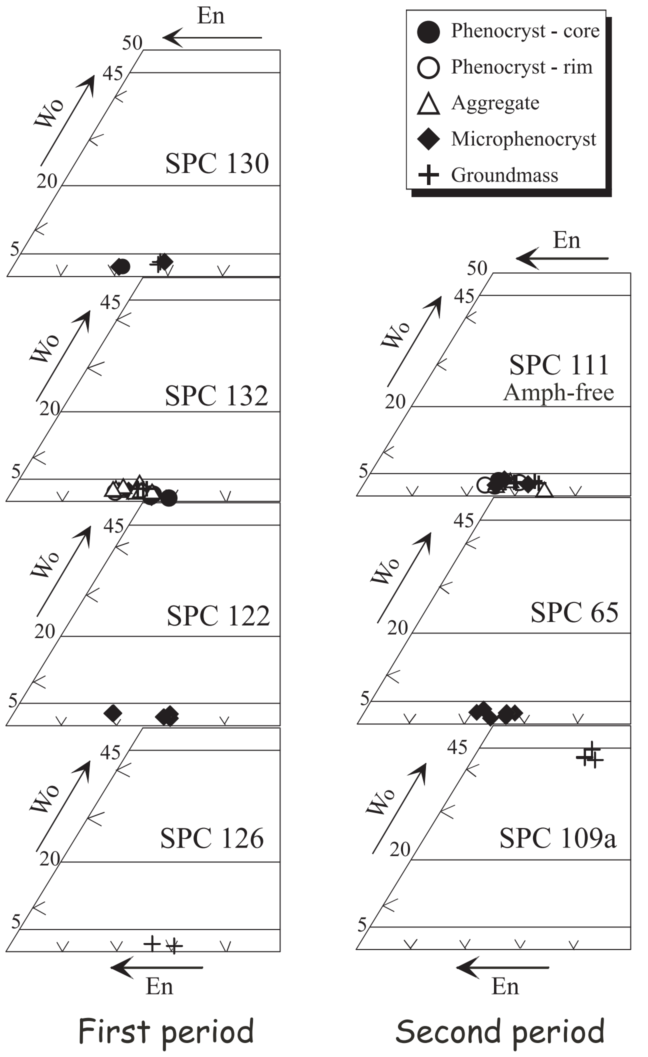

Figure 7. Quadrilateral component classification diagrams (Morimoto, 1989 et al.) for the pyroxene of the first and second San Pedro–Cerro Grande volcanic complex periods. Symbols: aggregate: aggregate of crystals. Wo = wollastonite; En = Enstatite.

Al-in-hornblende geobarometer. Calculations using data for the first-period amphibole yielded a pressure of 0.25 GPa, while for the second-period amphibole, pressures of 0.43–0.37 GPa were calculated. Considering the error in the calibration (±0.06 GPa, Johnson and Rutherford, 1989), the two values overlap, and their average translates to a depth of 13 km, assuming an average crustal density equal to that of an andesite rock column (2.7 g/cm^3).

The clinopyroxene geobarometer (Nimis, 1999) and the olivine-clinopyroxene geothermobarometer (Köhler and Brey, 1990) were applied to the magmatic inclusion hosted in the Amado Nervo lavas (sample SPC109), for which equilibrium between the coexisting olivine and clinopyroxene had been previously verified. The clinopyroxene geobarometer gives pressures of 1.68–1.78 GPa, which agrees with an estimated pressure of 1.76 GPa, assuming a temperature of 1225 °C, given by the olivine-clinopyroxene geothermobarometer. These results translate to a depth of 60 km.

The pre-eruptive magmatic temperature was evaluated using different geothermometers: Fe-Ti oxide (Ghiorso and Sack, 1991); plagioclase-amphibole (Holland and Blundy, 1994); Ca-in-orthopyroxene (Brey and Köhler, 1990); and olivine-clinopyroxene (Köhler and Brey, 1990).

Fe-Ti oxide thermometry was applied to first- and to second-period rocks (samples SPC122 and SPC65) of the amphibole-bearing group. Magnetite and ilmenite pairs used for estimates met the criterion for equilibrium based on Mn and Mg partition in the oxide phases (Bacon and Hirschmann, 1988). The results indicate a temperature of 830 °C for the first-period sample, and a lower temperature of 711 °C for the second-period rock. Oxygen fugacities calculated from these data are –11.19 and –13.72 log fO_2 (+2.05 and +2.26 ΔNNO), respectively (ΔNNO is Ni-NiO buffer).

Pre-eruptive temperatures for rocks of the amphibole-bearing group were also evaluated using the plagioclase-amphibole thermometer. Plagioclase and amphibole rim compositions yielded edenite-richterite exchange temperatures of 770–880 °C for the high-silica dacites of the first-period rocks, 870–920 °C for andesite and low-silica dacite of the first-period rocks, and 800–860 °C for the second-period rhyolites, using the range of pressures determined already. These results agree with those from the Fe-Ti oxides for the first-period rocks, but plagioclase-amphibole temperatures for second-period rocks are higher than those from Fe-Ti oxides.

The Ca-in-orthopyroxene geothermometer invariably yields higher temperatures than those of the other two geothermometers, in the pressure ranges obtained herein. Indeed, first- and second-period dacite-rhyolites yielded temperatures in the range of 900–980 °C, whereas less evolved compositions of first-period rocks gave higher temperatures in the range of 980–1074 °C, confirming the slightly higher temperatures as shown by the amphibole-plagioclase thermometer. This is in agreement with the lower degree of evolution (i.e., lower silica contents) shown by the first-period rock (i.e., sample SPC130) with respect to the first- and second-period rocks (i.e., SPC122 and SPC65). The higher temperatures obtained by the Ca-in-orthopyroxene thermometer may reflect higher closing temperatures for pyroxene in comparison to magnetite and ilmenite, a discrepancy already reported by other authors (e.g., Matthews et al., 1994; Schmitt et al., 2001).

The Ca-in-orthopyroxene geothermometer was also applied to amphibole-free rocks, for which other geothermometers could not be used (i.e., sample SPC111). The results indicate temperatures in the range of 1018–1080 °C, assuming the same pressure as for the amphibole-bearing rocks. These temperatures fall in the range of less evolved first-period amphibole-bearing rocks, obtained with the same geothermometer, in accordance with the less evolved composition shown by this amphibole-free rock.

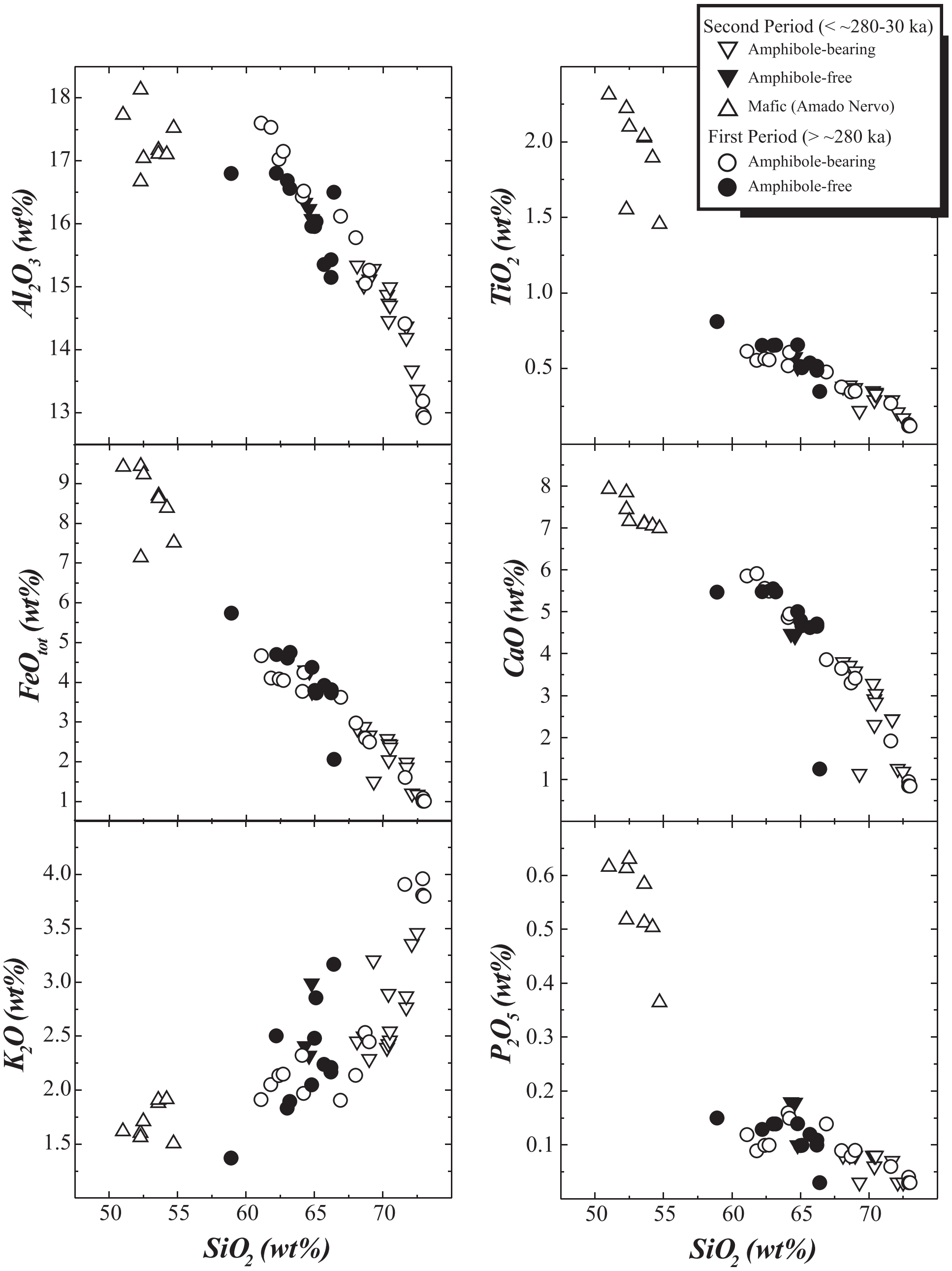

Figure 8. Variation diagrams for Al_2O_3, TiO_2, FeO_{tot}, CaO, K_2O, and P_2O_5 versus SiO_2 for San Pedro–Cerro Grande volcanic complex rocks.

The plagioclase-melt geohygrometer (Housh and Luhr, 1991) was used to constrain the pre-eruptive water contents of amphibole-bearing and amphibole-free rocks. Following the experimental calibration of Housh and Luhr (1991), we consider only the results which did not exceed 0.4 wt% H_2O of difference between the Ab and An calibration. Water contents in amphibole-bearing rocks were calculated at 0.35 GPa and 830 °C and ranged as follows: first-period dacites 6.5–6.8 wt% H_2O Ab and 6.4–6.7 wt% H_2O An, and 7.9 wt% H_2O Ab and 8.2 wt% H_2O An; second-period rhyolites 7.0 wt% H_2O Ab and 6.7 wt% H_2O An. Thus, an average value of ~7 wt% H_2O can be estimated for amphibole-bearing rocks. Considering the higher temperature of ~900 °C given by the Ca-in-orthopyroxene geothermometer, the estimated water contents are lower (~5–6 wt% H_2O), but still high in comparison with those calculated by Carmichael (2002) for Colima andesites.

Water contents were estimated for amphibole-free rocks assuming a total pressure equal to that for the other group and two values of temperatures: 1050 °C and 830 °C. The higher temperature is the average calculated for this group with the Ca-in-orthopyroxene geothermometer, whereas the lower temperature is the average for the amphibole-bearing group. These two values were used to overcome the poor temperature estimate, which in this case was based only on one sample. Water contents

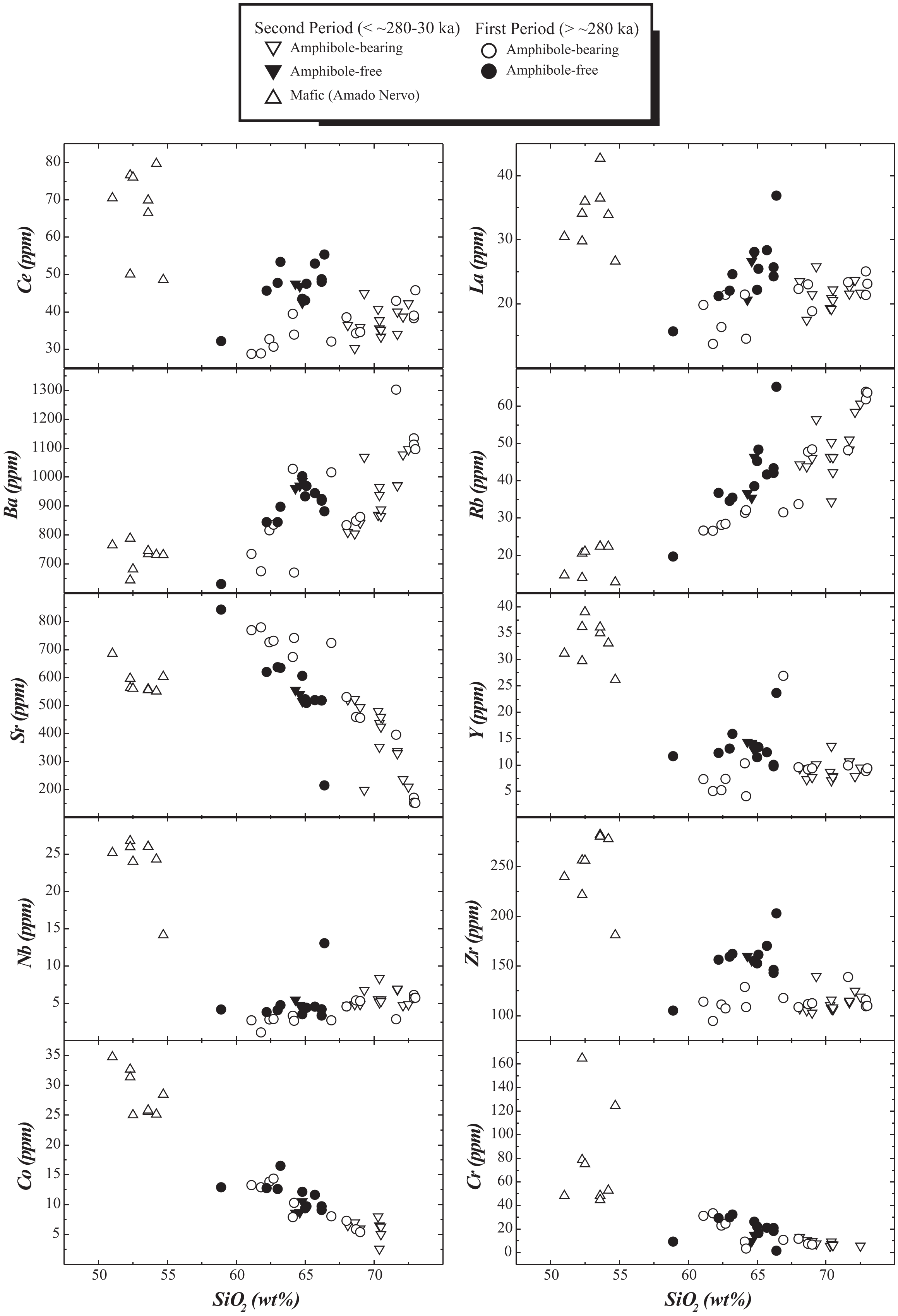

Figure 9. Variation diagrams for Ce, La, Ba, Rb, Sr, Y, Nb, Zr, Co, and Cr versus SiO_2 for San Pedro–Cerro Grande volcanic complex rocks.

in the amphibole-free group thus yielded 2.8–2.9 wt% H_2O Ab and 2.9 wt% H_2O An at 1050 °C, and 7.3–7.5 wt% H_2O Ab and 7.6–7.7 wt% H_2O An at 830 °C. These latter values overlap those observed for the amphibole-bearing rocks.

If our estimated water contents are correct, they represent the highest water content obtained for intermediate Quaternary rocks in the rear part of western Trans-Mexican Volcanic Belt. In fact, andesite and dacites from Ceboruco, Tequila, San Juan, and Colima volcanoes have a maximum 5% water content (Luhr, 2000; Carmichael, 2002). On the other hand, such high water estimates may reflect our poorly constrained temperature estimates.

WHOLE-ROCK COMPOSITIONS

Despite the differences between the Na-alkaline mafic Amado Nervo rocks on one hand, and intermediate to felsic subalkaline rocks on the other, well-correlated trends from the more mafic compositions to the more felsic ones are shown on plots of FeO_{tot} and CaO versus silica contents (Fig. 8). All other major-element abundances (Al_2O_3, TiO_2, K_2O, and P_2O_5), however, show a poor correlation with silica contents. Amado Nervo rocks are enriched in all major elements, with the exception of K_2O and SiO_2, if compared with intermediate-felsic rocks. We observe a compositional gap from 55 to 60 wt% silica between Amado Nervo and intermediate-felsic rocks. No significant differences exist between intermediate to felsic rocks of the two periods on the basis of major elements.

Trace-element patterns show a different picture (Fig. 9). Amado Nervo rocks plot quite differently from intermediate-felsic rocks, and do not represent any typical comagmatic end member. In addition, Amado Nervo rocks are enriched in the light rare earth elements (LREE), high field strength elements (HFSE), and compatible elements, and they are depleted in Ba and Rb contents in comparison to intermediate-felsic rocks (Fig. 9). Hygromagmatophile element patterns (Fig. 10) are characterized by low LILE/HFSE (large ion lithophile elements) and LREE/HFSE ratios, intermediate between those of calc-alkaline and oceanic-island basalt suites (i.e., "transitional series" of Petrone et al., 2003).

The petrographic twofold subdivision already highlighted for intermediate to felsic rocks is strictly reflected in whole rock compositions of these samples. Indeed, amphibole-free rocks are characterized by higher Ce, La, Ba, Rb, Y, Zr, and slightly lower Sr contents, whereas amphibole-bearing rocks have lower Ce, La, Ba, Rb, Y, and Zr contents and higher Sr at the same silica contents. No significant differences are observed among these two groups in the hygromagmatophile element patterns (Fig. 10); these are characterized by depletions in Ta, Nb, and Ti, and high LILE/HFSE and LREE/HFSE ratios. Given this correlation between geochemical and petrographic characteristics, we prefer to use the petrographic distinction between amphibole-free and amphibole-bearing groups, which also implies the geochemical twofold subdivision. It is important to stress that the two groups span the two periods without significant geochemical differences among different periods in the same group.

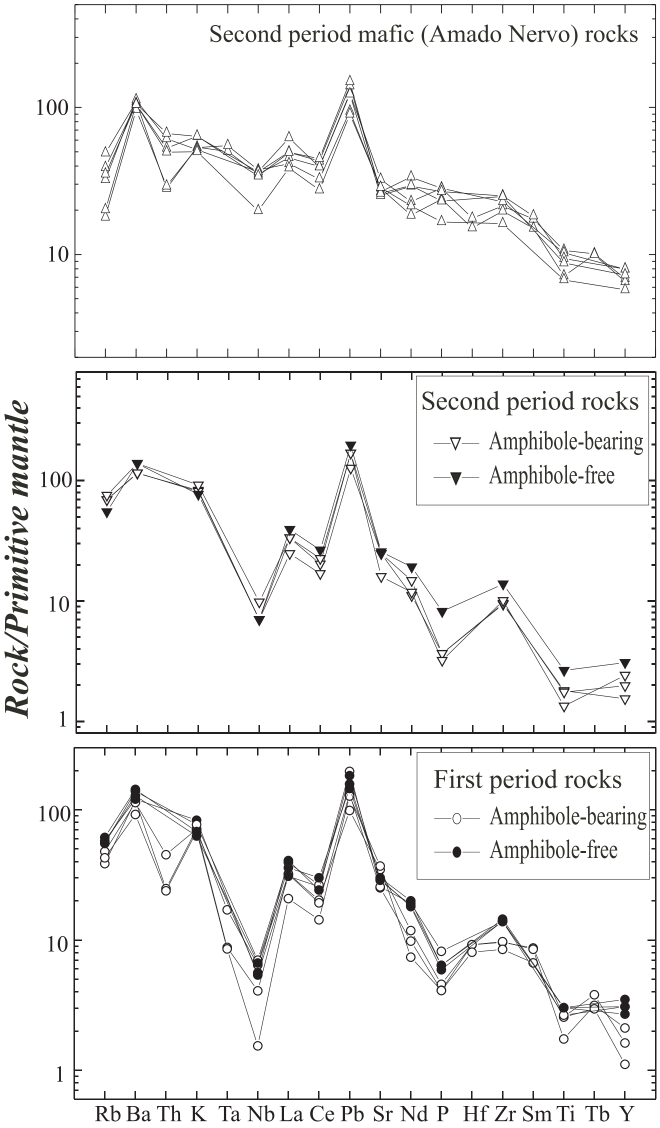

Figure 10. Patterns of hygromagmatophile elements normalized to primitive mantle (Sun and McDonough, 1989) for San Pedro–Cerro Grande volcanic complex rocks.

All studied rocks plot in the depleted Sr and Nd quadrant in the ε_{Nd} versus $^{87}Sr/^{86}Sr$ plot (Fig. 11). The Amado Nervo transitional rocks straddle the western Trans-Mexican volcanic Na-alkaline and calc-alkaline fields, whereas intermediate to felsic amphibole-bearing rocks fall in the field of calc-alkaline rocks from the western Trans-Mexican Volcanic Belt.

Amado Nervo rocks have lower $^{87}Sr/^{86}Sr$ (0.70351–0.70388) and higher ε_{Nd} values (4.3–5.7) with respect to all intermediate to felsic subalkaline rocks (Table 11, Fig. 11). Amphibole-bearing rocks show quite a large range of $^{87}Sr/^{86}Sr$ values, which

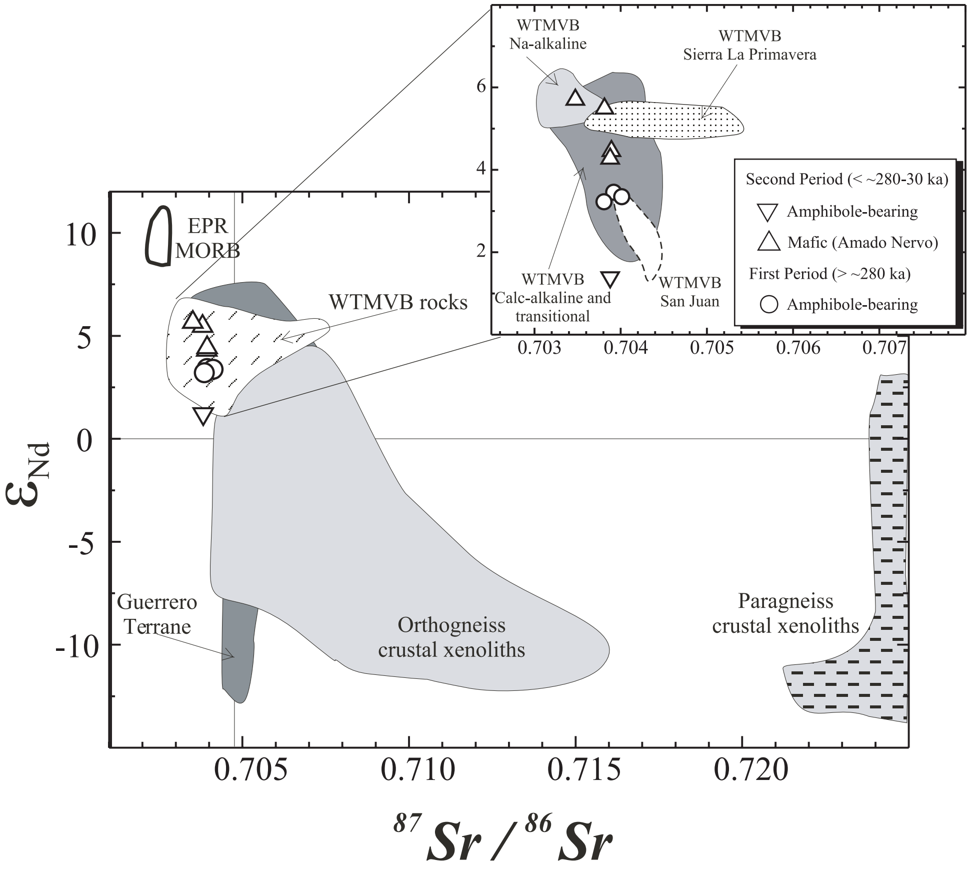

Figure 11. ε_{Nd} versus $^{87}Sr/^{86}Sr$ diagram for the amphibole-bearing and Amado Nervo rocks. Fields are based on data from: East Pacific Rise (EPR) and Gulf of California mid-ocean-ridge basalts (MORB) (Saunders, 1982; Smith, 1999); orthogneiss crustal xenoliths (Cameron et al., 1992); paragneiss crustal xenoliths (Cameron et al., 1992); Guerrero terrane (Centeno-García et al., 1993); and western Trans-Mexican Volcanic Belt (WTMVB) rocks: WTMVB Na-alkaline (Verma and Nelson, 1989a, 1989b; Righter et al., 1995; Petrone et al., 2003), WTMVB calc-alkaline and transitional (Luhr et al., 1989; Verma and Nelson, 1989a, 1989b; Wallace and Carmichael, 1994; Righter et al., 1995; Luhr, 1997; Petrone et al., 2003), WTMVB Sierra La Primavera (Mahood and Halliday, 1988); and WTMVB San Juan (Luhr, 2000).

nearly overlap the higher values of Amado Nervo rocks (Fig. 12). On the other hand, amphibole-free rocks are characterized by the highest $^{87}Sr/^{86}Sr$ ratios (0.70411–0.70424), which are also significantly higher than those of the amphibole-bearing group (0.70382–0.70401) (Fig. 12). No systematic differences in Sr and Nd isotope ratios are observed among intermediate to felsic rocks from different periods. $^{87}Sr/^{86}Sr$ ratios of Amado Nervo rocks do not correlate with SiO_2 or Rb contents, whereas they show a subtle positive correlation with Ce (Fig. 12). $^{87}Sr/^{86}Sr$ ratios of amphibole-bearing rocks show a negative correlation with silica, Ce, and Rb contents (Fig. 12).

DISCUSSION

Amphibole-free and amphibole-bearing subalkaline rocks span the entire period of activity of the San Pedro–Cerro Grande volcanic complex, whereas mafic Na-alkaline Amado Nervo rocks are subordinate and confined to the final period of activity. Although, subalkaline and Na-alkaline magmas have been outpoured almost from the same plumbing system, no evidence of magma interaction between these two extreme types of magmas is observed. Petrographic, chemical, and isotopic characteristics of all these three groups indicate that each group underwent different evolution processes. Magmatic enclaves are commonly hosted by amphibole-bearing rocks, whereas they are scarce in the amphibole-free products. They have the same petrographic and mineralogical composition of the hosting dacitic rocks, suggesting crystallization from felsic magma similar to the host. In the following section, we will discuss magma evolution of intermediate to felsic subalkaline and Na-alkaline rocks separately, before proposing a comprehensive petrologic model for the entire San Pedro–Cerro Grande volcanic complex.

Intermediate to Felsic Rocks

Amphibole-bearing and amphibole-free rocks do not belong to the same line of magmatic descent, despite their close association in time and space. They contain different mineralogical phases at the same silica contents and also show different correlation trends on silica versus major- and trace-element plots. Finally, they are characterized by significantly different $^{87}Sr/^{86}Sr$ ratios. Trace-element data show that these two groups of rocks follow separate lines of descent. However, the least evolved samples of each subalkaline group of rocks display similar trace-element contents, suggesting they were derived from a common parental magma.

Given the high water content estimates for these rocks (5–7 wt% H_2O for amphibole-bearing and probably lower for amphibole-free), the andesite water-saturated phase diagram

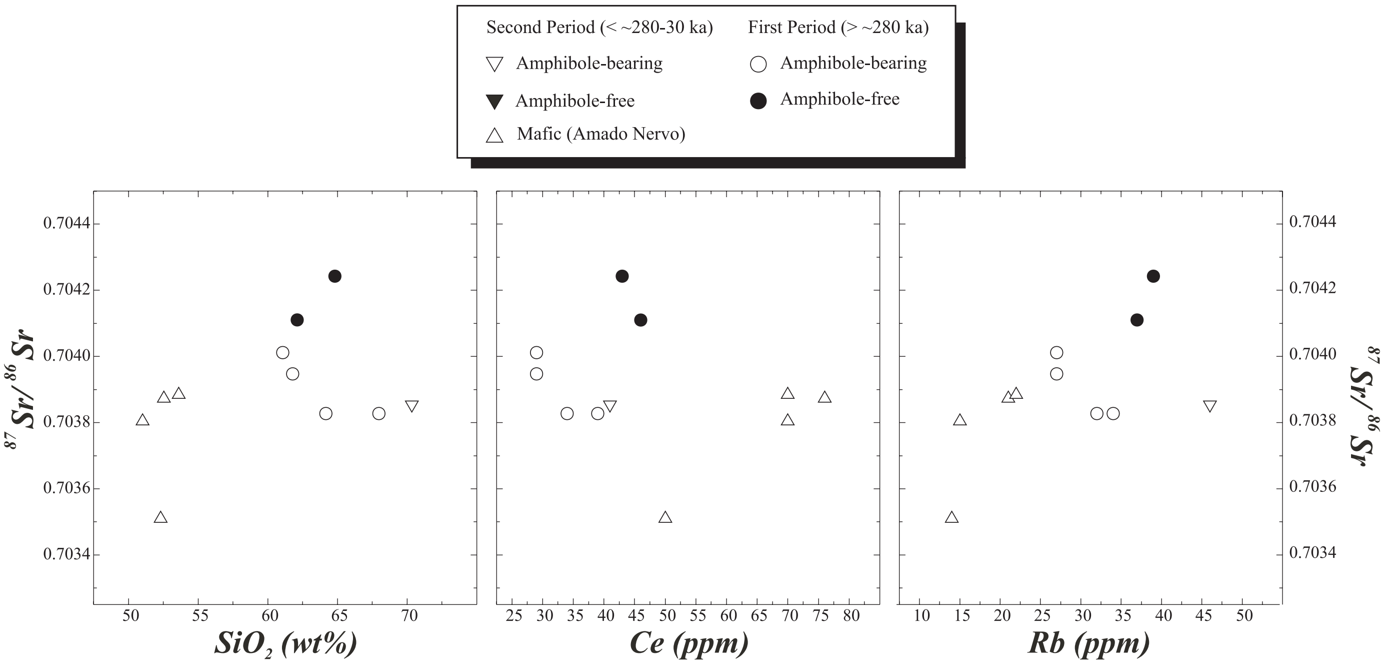

Figure 12. Variation diagrams of $^{87}Sr/^{86}Sr$ versus SiO_2, Ce, and Rb for San Pedro–Cerro Grande volcanic complex rocks.

(Moore and Carmichael, 1998) gives insights on their mineral phase relationships. In particular, at high pressure >~0.2 GPa and moderate temperature (≤950 °C), hornblende and plagioclase (±magnetite and pyroxene) are the stable phases at high water contents (5–7 wt%). With decreasing pressure (and dissolved water content), hornblende is no longer stable and plagioclase (±magnetite and pyroxene) is the dominant phase. Thus, starting from a common hydrated parental magma, different mineralogical assemblages can be generated.

The lack of mafic subalkaline end members in the San Pedro–Cerro Grande volcanic complex might be explained by the presence of large magma chambers in which evolutionary processes drive toward intermediate and felsic compositions. An alternative hypothesis might be the possibility that andesite and dacite magmas can also be generated by partial melting of the lower crust. Well-correlated trends shown by major and trace elements of amphibole-free and amphibole-bearing groups, which constitute two continuous series from high-silica andesite to rhyolite, indicate that fractional crystallization processes have played an important role in producing the observed chemical and mineralogical characteristics shown by these rocks. In this light, partial melting processes represent a mere possibility of secondary importance. On the other hand, simple crystal fractionation cannot explain the observed $^{87}Sr/^{86}Sr$ isotope variations (Fig. 12) in both amphibole-free and amphibole-bearing groups. The observed differences in isotope compositions in both groups might be related to crustal contamination processes.

The composition of the middle and lower crust in our study area is not well known. The Puerto Vallarta Cretaceous batholith (Schaaf et al., 2000) may underlie the area (Ferrari et al., 2003), where the batholith is supposed to have intruded Mesozoic volcanic and sedimentary sequences of the Guerrero terrane (e.g., Centeno-García et al., 1993). However, Schaaf et al. (2003) indicated the presence of an older, pre-Guerrero, midlower crustal basement in the area. The geochemical nature of this basement is unknown, and we assume that lower-crustal paragneiss and orthogneiss granulite-facies xenoliths reported by Ruiz et al. (1988) for central México might also constitute the basement in western México. All possible crustal contaminants are characterized by Sr isotope ratios higher than our assumed initial magma (Fig. 11), and thus the particular signature left in rock compositions involved in an assimilation plus fractional crystallization (AFC) process should be the positive correlation of Sr isotope ratios versus evolutionary parameters (De Paolo, 1981), as observed for the amphibole-free rocks. A different type of crustal contamination process is represented by the so-called assimilation plus equilibrium crystallization processes (AEC; Huppert and Sparks, 1985; Devey and Cox, 1987). In this model, different batches of magma, characterized by various degrees of evolution, are able to assimilate different amounts of crustal rock, depending on their temperatures.

In detail, mafic magmas that have higher temperatures will be able to assimilate a greater amount of wall rock than cooler silicic magmas. The result is a greater change in Sr isotope ratios for more mafic than for more evolved magmas. By this process, a negative correlation of Sr isotope ratios versus degree of evolution can develop, as is the case of the amphibole-bearing rocks. Assimilation can occur either in the magma chamber or during magma ascent (Huppert and Sparks, 1985; Devey and Cox, 1987; Peccerillo and Wu, 1992; Francalanci and Santo, 1993; Francalanci et al., 1993). Thus, it is clear that different types of crustal contamination processes will result in different relationships between Sr isotope ratios and other evolutionary parameters, as is the case for the amphibole-free and the amphibole-bearing rocks.

Amphibole-Free Group

The observed $^{87}Sr/^{86}Sr$ isotope variations, with silica-rich rocks having higher $^{87}Sr/^{86}Sr$ values (Fig. 12), might be related to crustal assimilation acting in concert with crystal fractionation. AFC processes (De Paolo, 1981) were modeled using the less evolved amphibole-free rock (SPC146) as the parental magma composition, and assuming a Sr isotopic composition equal to the least radiogenic value (0.70382) found in San Pedro–Cerro Grande volcanic complex felsic rocks. Results of the modeling are shown in Figure 13. On the basis of Sr isotope data, it is possible to constrain reasonable r (ratio of assimilation rate to crystallization rate) values between 0.1 and 0.5 for the paragneiss composition (mean 0.3). This composition seems to better match the variability shown by the isotopic data. On the other hand, unreasonably high r values of 0.8–0.85 are obtained using the orthogneiss composition as a possible crustal contaminant. This suggests that the paragneiss composition is a more likely contaminant than the orthogneiss. Thus, trace elements were modeled using the paragneiss composition. The bulk partition coefficients for the trace elements used in the modeling were evaluated on the basis of the mode of the rocks and supported by fractional crystallization calculations, which were undertaken in order to get at least some qualitative indications on the proportions of crystallizing mineralogical phases. The fractional crystallization calculations indicated separation of plagioclase (~62%), orthopyroxene (~30%), and titanomagnetite (~8%) in proportions similar to the observed modes. Starting from this, we evaluated bulk partition coefficients for the modeled trace elements using values from the literature (Francalanci and Santo, 1993) suitable for intermediate-felsic subalkaline rocks. AFC processes were modeled using fixed bulk partition coefficients for the different elements and variable r values, which gave a grid in the element versus element plot of Figure 13. AFC processes characterized by various combinations of r values and degrees of solid fractionation (S) fit quite well the variation trends observed for trace elements of the second-period amphibole-free rocks. First-period rocks were more problematic, although most of the observed variation trends may still be explained by AFC processes. High degrees of fractionation need to be invoked in order to explain the generation of the first-period rock, which lies outside the observed trend, but has the lowest Sr content and is the most evolved (Fig. 13). AFC processes can also explain the element variation observed in first-period amphibole-free rocks, which show deviations in Sr versus Ba and Zr plots (Fig. 13). High r values (>0.6) would be needed to match the observed Sr compositional trends on a line for a high bulk Sr partition coefficient. On the other hand, these first-period rocks are almost aphyric, and it is possible that mineral phase proportions are slightly different for these rocks compared to other first- and second-period rocks. Lower amounts of plagioclase would be enough to lower the bulk Sr partition coefficient to a value that would produce a line of low constant r (~0.2), matching the trend observed for these rocks.

The modeling suggests that the evolution of the amphibole-free magmas is controlled by AFC processes, characterized by different r values. A range of r values is expected, since samples were collected from different domes and each magma had a different history of ascent. The mass of fractionating solid also varies, but is around 10%–30% for all modeled trace elements, with probably a smaller range (~10%–20%) for the first-period aphyric rocks. These figures are in agreement with the Sr isotope data, which suggest a value of 10% for fractionating solid.

Amphibole-Bearing Group

The amphibole-bearing group shows a large range in isotope ratios and no clear correlation between $^{87}Sr/^{86}Sr$ ratios and ε_{Nd} values (Fig. 11). First-period rocks have almost constant ε_{Nd} values but a wider range in $^{87}Sr/^{86}Sr$ ratios. One of the second-period samples is instead characterized by a significantly lower ε_{Nd} value. In addition, a negative correlation between Sr isotope ratios versus degree of evolution is noticeable (Fig. 12). All these observations can be interpreted in the light of AEC processes.

In order to evaluate whether AEC processes might explain the geochemical and isotopic characteristics of the investigated rocks, crustal contamination and mixing calculations were undertaken to model such processes. Since AEC processes act on liquids having different degrees of evolution, it is necessary to evaluate the role of fractionation in modifying major- and trace-element contents of this group of rocks. Simple crystal-fractionation calculations were performed using quantitative major-element mass-balance modeling and assuming the composition of SPC124 as the parental liquid composition. This sample has the lowest silica content and the highest concentration of compatible trace elements of the amphibole-bearing group. Thus, it appears to be the closest derivative from a more primitive magma composition among the amphibole-bearing group.

Two steps of fractionation were evaluated. The first step considers evolution from andesite to dacite, whereas the second step covers evolution of dacite to rhyolite. The fraction-

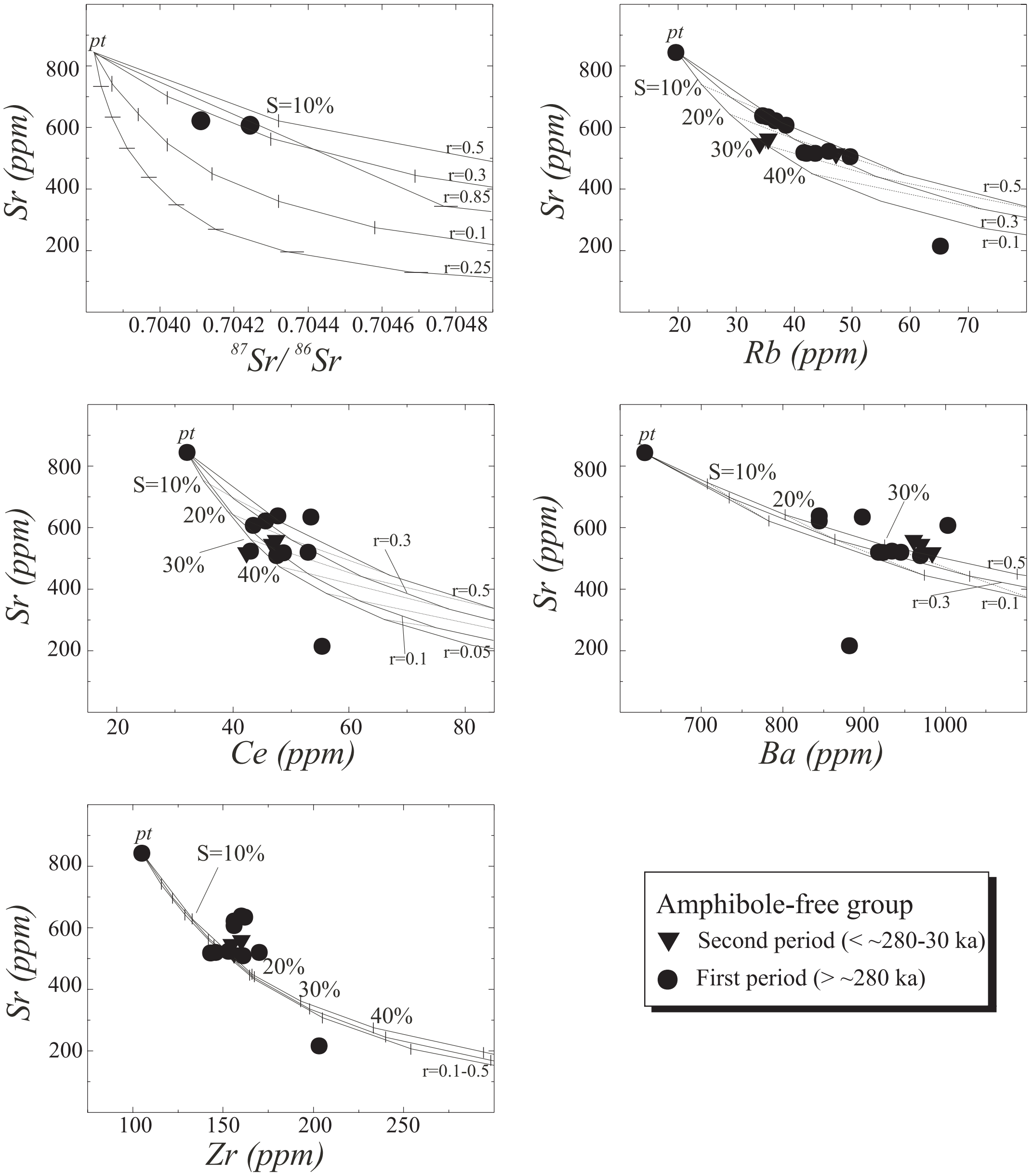

Figure 13. Sr versus $^{87}Sr/^{86}Sr$, Rb, Ce, Ba, and Zr showing the results of assimilation and fractional crystallization (AFC) processes for the amphibole-free rocks using two different compositions of crustal xenoliths: orthogneiss (MN42, Cameron et al., 1992; line with horizontal bars) and paragneiss (GNX22, Cameron et al., 1992; line with vertical bars). Symbols on lines or thin lines represent different amounts of S = solid fractionation (S = 10%–20%–30%). AFC processes were modeled using different *r* (= assimilation rate/crystallization rate) values and bulk partition coefficients: $D^{Sr} = 2$; $D^{Rb} = 0.02$; $D^{Ce} = 0.4$; $D^{Ba} = 0.04$; $D^{Zr} = 0.2$. Partition coefficients were taken from Francalanci and Santo (1993). Hypothetical initial magma composition (pt): $^{87}Sr/^{86}Sr$: 0.703821; other element values as in sample SPC146.

ating mineral assemblages were selected, using those phases that produced the smallest residual errors (Σr^2, squared oxide wt%). Andesite to dacite crystal fractionation can be modeled by fractionating around 31% solid, constituted by plagioclase (59%), amphibole (28%), orthopyroxene (7%), and titanomagnetite (7%). The dacite-rhyolite path can be modeled by 20% crystallization of plagioclase (56%), amphibole (40%), titanomagnetite (3%), and apatite (1%). The residual errors are low in both cases (0.1 and 0.4, respectively), and the fractionating assemblages agree with the observed mineral modal compositions of the rocks.

Trace-element modeling for selected elements (Cr, Co, Rb, Sr, Y, Nb, Zr, Ba, La, and Ce) was performed using Rayleigh fractionation. The partition coefficients were taken from the literature (Francalanci and Santo, 1993) and evaluated for being suitable for intermediate-felsic subalkaline rocks. Results indicate that the calculated Ce contents agree with observed values, suggesting that amphibole played a key role in determining contrasting Ce contents in amphibole-bearing and amphibole-free groups. Fractional crystallization fails to match the observed variations for all other trace elements. This was expected given the large Sr isotope variability, which points to the assimilation of continental crust. In particular, the Sr enrichment (element concentration in liquid/initial element concentration) is lower than any modeled enrichment, whereas it is always higher for Rb.

The observed variations in the ε_{Nd} versus ^{87}Sr/^{86}Sr diagram (Fig. 11) indicate that at least two different crustal compositions were involved in the evolution of the amphibole-bearing rocks. These crustal components are characterized by having different ^{143}Nd/^{144}Nd and ^{87}Sr/^{86}Sr compositions. Mexican crustal components span large ranges in composition and in many cases one of the components is not clearly distinguishable from the others, given their overlapping isotopic compositions (Fig. 11). Nevertheless, the observed Nd and Sr isotope compositions of the amphibole-bearing rocks allow us to discriminate among different crustal compositions. One of the crustal components should be characterized by high ^{87}Sr/^{86}Sr ratios, low Sr contents, and relatively high ε_{Nd} values, close to those shown by the first-period amphibole-bearing rocks. The most probable candidates with such a composition are either orthogneiss or paragneiss crustal xenoliths from central and eastern México (Cameron et al., 1992). The other component should be characterized by low ε_{Nd} values and ^{87}Sr/^{86}Sr ratios. This component could be either orthogneiss or the Jurrassic-Cretaceous volcano-sedimentary sequence, which constitutes the upper part of the Guerrero terrane, hosting the Puerto Vallarta batholith (Centeno-García et al., 1993).

AEC processes were evaluated using both Sr and Nd isotope data and selected incompatible trace-element data (Fig. 14). The increase in ^{87}Sr/^{86}Sr ratios without a concurrent decrease in Nd isotope ratios (Fig. 14A), observed for high ^{143}Nd/^{144}Nd and high ^{87}Sr/^{86}Sr first-period rocks, is matched by adding different amounts of crustal contaminants (maximum amount <20%), such as either orthogneiss or paragneiss. In this case, the composition of the paragneiss would be completely different from that previously used for modeling AFC processes for the amphibole-free rocks. This seems highly improbable considering the limited area in which both groups were erupted, and thus suggests that the orthogneiss is a more probable candidate as the crustal contaminant. The decrease in ^{143}Nd/^{144}Nd associated with a slight increase in ^{87}Sr/^{86}Sr ratios shown by post-caldera second-period rock is matched by crustal contamination (~5%–10%) from the Jurassic-Cretaceous sequence of the upper part of the Guerrero terrane. This contamination could also have originated from a hypothetical orthogneiss with a composition that is different from the orthogneiss mentioned earlier. This case would imply the existence of an extremely heterogeneous orthogneiss for which evidence is still lacking.

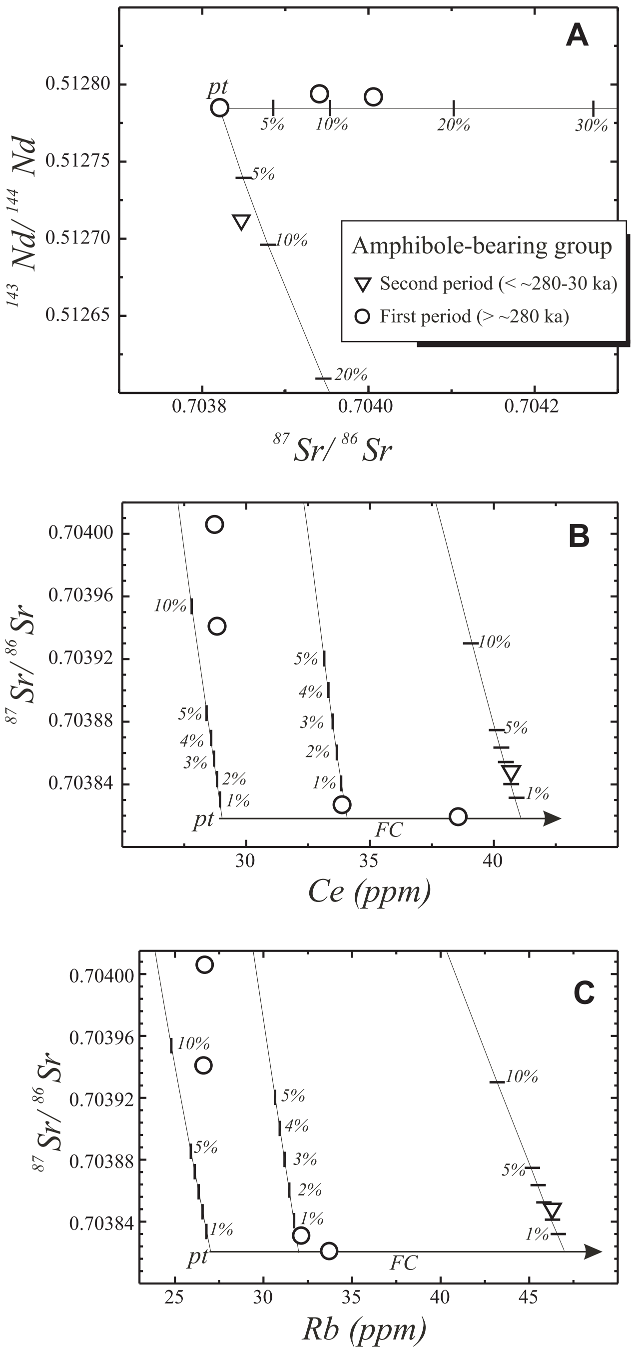

Figure 14. (A) ^{143}Nd/^{144}Nd versus ^{87}Sr/^{86}Sr; (B) ^{87}Sr/^{86}Sr versus Ce; and (C) ^{87}Sr/^{86}Sr versus Rb diagrams for amphibole-bearing San Pedro–Cerro Grande volcanic complex rocks, showing the results of assimilation and equilibrium crystallization (AEC) modeling. AEC was modeled starting from liquids at different degrees of evolution. Lines plus symbols are mixing lines modeling the crustal assimilation processes between the hypothetical parental magma (*pt*: ^{143}Nd/^{144}Nd 0.512785; ^{87}Sr/^{86}Sr 0.703821; Sr 780 ppm; Nd 13 ppm; Ce 29 ppm; and Rb 20 ppm) and different compositions of Mexican crustal rocks: orthogneiss crustal xenolith (MN42, Cameron et al., 1992; line with vertical bar) and Guerrero terrane (G8-90; Centeno-García et al., 1993; line with horizontal bar). Numbers on line indicate different percent of mixing. FC = fractional crystallization. More details are given in the text.

Starting from the hypothetical composition of the parental magma, which has the lowest observed incompatible trace-element contents and the lowest observed $^{87}Sr/^{86}Sr$ ratios, simple crystal fractionation would not modify Sr isotope ratios, but would produce an increase in incompatible trace elements (i.e., Ce and Rb), as shown in Figures 14B and 14C. The highest $^{87}Sr/^{86}Sr$ ratios displayed by the least-differentiated first-period rocks can be explained by orthogneiss crustal contamination. In this case, the highest $^{87}Sr/^{86}Sr$ ratio is produced by the greatest amount of crustal contamination (10%–20%). On the other hand, this mixing line does not match the lower $^{87}Sr/^{86}Sr$ ratio shown by the more differentiated first-period rocks. This would require a lower contamination of orthogneiss starting from a more differentiated liquid composition (Figs. 14B and 14C). The composition of the second-period rock is matched by less than 5% crustal contamination of an even more differentiated liquid (liquid with the same $^{87}Sr/^{86}Sr$ ratios as the initial parental magma, but higher Ce and Rb contents) by components from the Guerrero terrane. It might be argued that trace-element variation without concomitant changes in the $^{87}Sr/^{86}Sr$ ratios could also be the result of mantle source partial melting. The absence of a negative correlation between Nb and compatible elements, as well as the lack of any correlation among HFSE and HREE, speak against this hypothesis. Thus, although nonunique, these models, as well as those shown for the amphibole-free group, demonstrate that the chemical and isotopic composition of the studied rocks can be explained by different crustal contamination processes.

It is hard to say whether contamination took place during storage in a magma chamber or during ascent. The Al-in-hornblende barometer indicates mineral crystallization depths of around 13 km, which implies a mid- to upper-crustal magma chamber. Isotope data suggest the presence of two different crustal contaminants, which may be located at different depths in the crust (Cameron et al., 1992; Centeno-García et al., 1993). If crustal contamination took place in the magma chamber, we could expect a shallowing of the magma chamber with time from a deeper first-period to a shallower postcaldera reservoir. In principle, this might be possible, but clear evidence for this is not available. In this context, it seems to be more realistic to suggest that magmas having different degrees of evolution and slightly different temperatures, as suggested by geothermometer calculations (i.e., less evolved first-period rocks showing slightly higher temperatures than more evolved first- and second-period rocks), were generated by crystal fractionation processes, and that assimilation of crustal rocks mostly took place during the ascent of small magma batches feeding different domes. Several lines of evidence support this hypothesis: (1) the amounts of crustal assimilation depend upon the time factor in an evolving magma chamber. Under fractional crystallization and continuous availability of contaminant, the longer magmas remain in the chamber (i.e., more evolved magmas), the higher the contamination. This cannot apply to the amphibole-bearing rocks, for which less differentiated compositions are the more contaminated. (2) The high water contents of these magmas can favor partial melting of surrounding crustal rocks and thus their assimilation, which will be more efficient the smaller the batch of magma. (3) Water supply from magma degassing during ascent may favor partial melting of crustal rocks, thus favoring AEC processes even in more evolved magmas.

Amado Nervo Na-Alkaline Rocks

Amado Nervo lavas are unique in the San Pedro–Cerro Grande volcanic complex in that they are characterized by large variations in trace-element and isotopic compositions despite their narrow silica range. Olivine is the only phenocryst, and plagioclase, clinopyroxene, and opaque minerals are found solely in the groundmass, along with olivine. These petrographic characteristics are difficult to reconcile with the observed variations between silica and other major elements (Fig. 8). Indeed, TiO_2, Al_2O_3, CaO, and K_2O do not correlate positively with silica content, as would be expected for olivine-dominated fractionation. In addition, trace elements are scattered at the same silica content (Fig. 9). Amado Nervo rocks also have variable $^{87}Sr/^{86}Sr$ ratios, which are not correlated with silica or trace-element contents (Fig. 12). All these observations indicate that simple fractional crystallization cannot be responsible for the observed whole-rock data. Instead these variations could arise from crustal assimilation or source differentiation processes.

The negative correlation between Sr and K_2O contents (Fig. 15) might suggest crustal assimilation, which could also lead to the negative correlation between $^{143}Nd/^{144}Nd$ versus $^{87}Sr/^{86}Sr$ ratios and the positive correlation between $^{87}Sr/^{86}Sr$ and $^{206}Pb/^{204}Pb$ ratios (Fig. 15) (Petrone et al., 2003). On the other hand, this process is not clearly supported by the poor correlations between $^{87}Sr/^{86}Sr$ ratios and Rb, Sr, and silica contents. A crustal assimilation process (i.e., AFC) represents just one of the possible explanations for the correlation trends observed between Sr and Nd (i.e., a negative trend) and Pb isotopes (i.e., a positive trend). Furthermore, the rock (SPC24) with the highest Sr content (which should be the most contaminated and evolved magma if produced by an AFC process with no plagioclase fractionation), is neither characterized by the highest Rb and K_2O contents, nor by the most radiogenic $^{87}Sr/^{86}Sr$ and $^{206}Pb/^{204}Pb$ ratios nor by the lowest $^{143}Nd/^{144}Nd$ ratio (Fig. 15, Tables 3 and 11). In addition, the most primitive and least radiogenic sample (SPC25, based on Mg# and compatible trace elements) is not the most primitive in regard to incompatible trace-element abundances and silica content (Fig. 15, Tables 3 and 11). Thus, the relationships between trace elements and Sr, Nd, and Pb isotope data are difficult to explain by crustal contamination. The absence of a positive correlation between $^{87}Sr/^{86}Sr$ ratios and silica and incompatible elements speaks against an AFC process; the lack of a negative correlation excludes an AEC process.

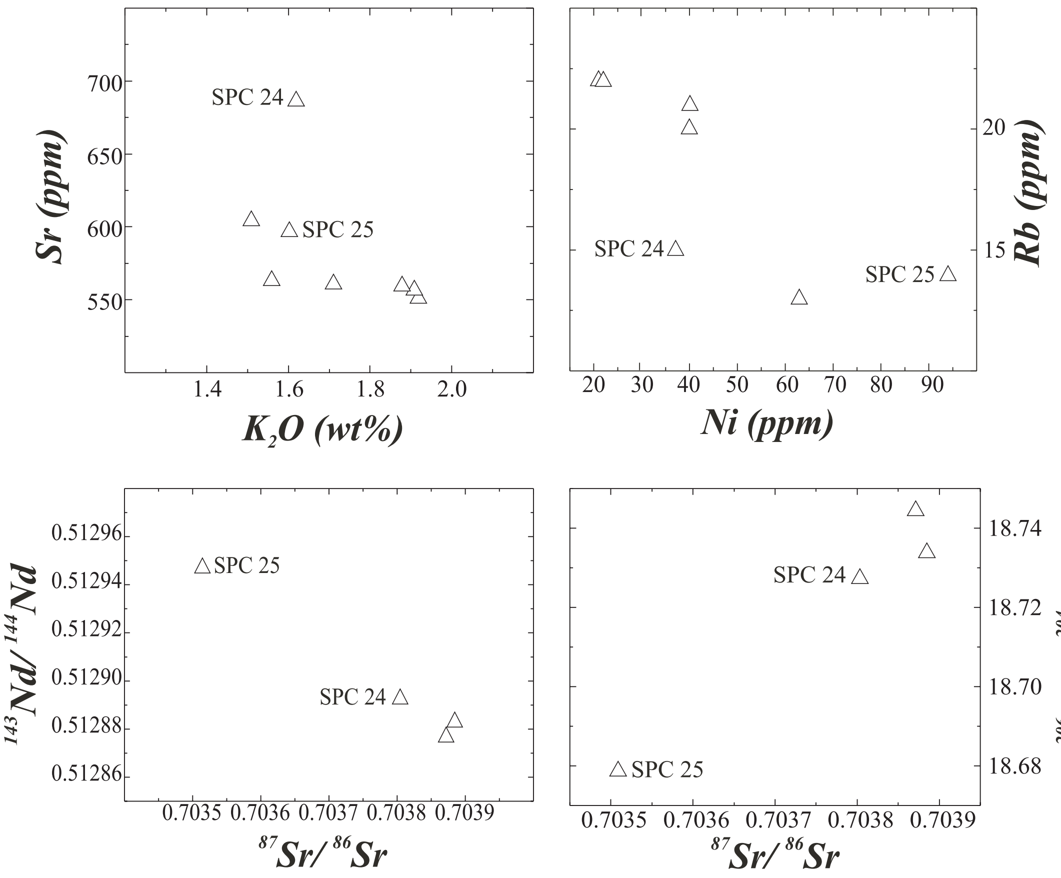

Figure 15. Sr versus K_2O; Rb versus Ni; $^{143}Nd/^{144}Nd$ and $^{206}Pb/^{204}Pb$ versus $^{87}Sr/^{86}Sr$ diagrams for the Amado Nervo rocks. Some samples are also labeled. See text for more details; $^{206}Pb/^{204}Pb$ data are from Petrone et al. (2003).

This evidence suggests that the observed variability in trace-element and isotope compositions was inherited from source processes. Geochemical and isotopic data suggest that the parental magma was only slightly modified by olivine fractionation. Clinopyroxene barometry of a magmatic enclave hosted in Amado Nervo lava indicates a depth of crystallization of around 60 km. This places the source of this magma in the upper mantle, since the mantle-crust boundary has been estimated at 40–50 km in this area (Urrutia-Fucugauchi and Flores-Ruiz, 1996). The observed variability in Sr, Nd, and Pb isotope compositions points toward a heterogeneous mantle source. The correlations observed between the three isotopic systems suggest variable degrees of mixing between different mantle components. Such an origin for these rocks was suggested before by Petrone et al. (2003), who showed that at least two mantle components (a depleted one and an enriched one) must exist in the mantle wedge below the San Pedro–Ceboruco graben. Mixing of partial melts from these two mantle sources may explain the observed isotopic compositions of mafic Amado Nervo rocks as well as their transitional affinity. At the same time, this heterogeneous mantle source might undergo variable degrees of partial melting, producing the observed compositional range in trace-element contents. Thus, the geochemical and isotopic characteristics of the Amado Nervo mafic rocks are most likely caused by variable degrees of partial melting of a heterogeneous mantle source.

Magma Evolution of the San Pedro–Cerro Grande Volcanic Complex

Petrographic, geochemical, and isotopic characteristics of the amphibole-free and amphibole-bearing rocks originated from different evolutionary processes that modified a common parental magma: AFC controlled the amphibole-free magmas and AEC controlled the amphibole-bearing magmas. The two magma series were contemporaneous but spatially separated (Fig. 5), suggesting the presence of at least two different magma storage regions.

The amphibole-bearing magma reservoir is probably located in the mid-upper crust. Unfortunately, it was not possible to constrain the depth of the amphibole-free reservoir from geothermobarometric calculations. Pre-eruptive magma temperatures for the amphibole-free magmas overlap those of the second-period amphibole-bearing rocks. Pre-eruptive water contents of amphibole-free magmas also overlap those for the amphibole-bearing group. Andesitic magmas with 7 wt% of water reach their solubility limit at ~0.3 GPa (Moore and Carmichael, 1998), thus water-saturated conditions fit better with estimated water contents and petrographic and chemical characteristics of intermediate to felsic rocks. The absence of amphibole crystallization suggests a magma reservoir that is shallower than that of the amphibole-bearing group. Magma in the shallower reservoir has also lower water contents because of decreasing water solubility at lower depth (Moore and Carmichael, 1998). Alternatively, amphibole-free magmas may have the same bulk composition and water contents as amphibole-bearing magmas, but they are hotter and thus beyond the thermal stability limit of amphibole. In this case, the two magma reservoirs might be at the same depth. Evidence is not enough to favor either one of these possibilities, but Al_2O_3 and Sr contents are higher in the amphibole-bearing than in the amphibole-free rocks, at the same silica contents. This indicates a limited role of plagioclase fractionation in the amphibole-bearing rocks. Plagioclase crystallization may be suppressed in a deeper reservoir, supporting the idea that the two magmas formed at different depths. In the water-saturated phase diagram for western México andesite (Moore and Carmichael, 1998), the lower stability field of mineral assemblages observed in amphibole-free and amphibole-bearing rocks is limited by the clinopyroxene-in curve. This mineral phase was not observed in our rocks. Furthermore, the diagram suggests lower pressure and lower water contents (<5 wt%) (and slightly higher temperature) for amphibole-free rocks. Thus, it seems possible that the amphibole-free magmas were more degassed and rested in a reservoir shallower than that of the amphibole-bearing magmas. Being stored in different reservoirs may have allowed the magmas to evolve through different crustal assimilation processes. Amphibole-bearing magma rested in a deeper (~0.3–0.4 GPa) reservoir where fractional crystallization allowed the formation of andesitic to rhyolitic liquids, which subsequently ascended as single magma batches with different degrees of evolution. Water exsolution subsequent to decompression degassing may have favored partial melting of crustal rocks of different types and thus AEC processes, which occurred during ascent. Amphibole-free magmas rested in a shallower reservoir characterized by lower amounts of water, and they evolved through AFC processes. The different eruptive styles displayed by the amphibole-bearing and amphibole-free magmas may have been the result of their different magma storage depths and water contents. Higher water contents of the amphibole-bearing magmas favored intense explosive activity, which resulted in the eruption of the Cuastecomate pumice deposit and subsequent San Pedro caldera collapse. The limited explosive activity produced by amphibole-free magmas (i.e., Las Cuevas pyroclastic deposit, which was probably related to the emplacement of a dome) may be related to their lower water contents. The amphibole-bearing and amphibole-free rocks are not highly crystalline, and hypohyaline lavas as well as aphyric rocks are found among them, respectively. This suggests rapid ascent toward the surface during the final part of the path, as also evidenced by the limited presence of amphibole reaction rims in amphibole-bearing rocks.

Within this frame, a mantle liquid with different petrological affinity unrelated to the typical subalkaline compositions (Petrone et al., 2003) of the San Pedro–Cerro Grande volcanic complex rose toward the surface during the second period of activity, giving rise to the Amado Nervo volcano. This volcano is located along the San Pedro caldera rim, indicating enhanced extensional crustal conditions in this area, which favored rapid ascent of magma from the mantle. A regime of long-term crustal extension in the region (Ferrari and Rosas-Elguera, 2000) favored the rising of this mafic liquid.

CONCLUSIONS

The volcanic evolution of the San Pedro–Cerro Grande volcanic complex can be divided into two main periods of activity. Highly viscous magmas were extruded in the form of coalescent domes and massive lava flows with minor pyroclastic eruptions. Formation of an ellipsoidal caldera divides the two periods of activity.

Precaldera volcanic activity is middle Pleistocene (younger than ca. 280 ka) in age and is characterized by the emplacement of subalkaline rocks ranging in composition from andesite to rhyolite. This first period ended before ca. 280 ka with the emplacement of the Cuastecomate Plinian deposit related to the formation of the San Pedro caldera. Postcaldera activity covers a time span between ca. 280 ka and 30 ka, with emplacement of subalkaline rocks, ranging from dacite to rhyolite, and minor Na-alkaline mafic rocks (hawaiite and mugearite). These two different types of magma are genetically unrelated to each other (Petrone et al., 2003) and no evidence of interaction between them has been found, suggesting that Na-alkaline hawaiites represent a separate pulse of magma from a different source.

Geochemical characteristics of the Na-alkaline Amado Nervo rocks suggest that source differentiation processes played an important role and that chemical compositions of the rocks were modified only slightly by low-pressure evolution processes. The extensional stress field characterizing the San Pedro–Cerro Grande volcanic complex area favored the rise of these mantle melts.

The subalkaline suite can be further divided into amphibole-bearing and amphibole-free rocks, which occur in both pre- and postcaldera periods. These two groups are coeval but spatially separated. Amphibole-bearing rocks have lower Ce and other related incompatible trace-element contents (i.e., La, Zr, Y, Rb) but higher Sr abundances than amphibole-free rocks.

Initial ^{87}Sr/^{86}Sr isotope values of amphibole-bearing rocks are lower than those of amphibole-free rocks.

Amphibole-bearing and amphibole-free magmas evolved in distinct reservoirs at different pressures and water contents. Amphibole-bearing magmas evolved at pressures between 0.3 and 0.4 GPa, in a magma chamber at ~13 km depth. Amphibole-free magmas evolved in a shallower magma chamber, characterized by lower water contents. All data suggest that these two groups of magmas were generated from a common hydrated parental magma that fed the two different reservoirs.

Amphibole-bearing magmas evolved by AEC processes, where fractionating phases included plagioclase, amphibole, orthopyroxene, and titanomagnetite. In addition, the assimilation of lower-crustal rocks kept Sr isotopic values low in contrast to Sr isotope ratios measured in amphibole-free rocks. High magmatic water contents favored partial melting of crustal rocks during ascent, and in turn determined AEC processes.

Amphibole-free magmas evolved by AFC processes with crystallization and fractionation of plagioclase, orthopyroxene, and titanomagnetite, and assimilation of middle-upper crustal metasedimentary rocks (i.e., paragneiss). In addition, amphibole-free magmas rose to the surface through a different plumbing system from the one used by the amphibole-bearing magmas. Eruption vents of amphibole-free rocks are concentrated to the southeast of the San Pedro–Cerro Grande domes.

Different depths of magma storage and water contents determined magma evolution paths producing either amphibole-bearing or amphibole-free magmas. Higher water contents in the deeper amphibole-bearing magmas may have favored a more intense explosive activity, which culminated in the San Pedro caldera collapse.

ACKNOWLEDGMENTS

The authors would like to thank the staff of the Laboratorio Universitario de Geoquímica Isotópica (LUGIS) of México, and in particular Gabriela Solis and Juan Julio Morales for allowing access to mass spectrometer facilities of the Universidad Nacional Autónoma de México (UNAM) in México City; Giulia Perini for help during the isotope analyses at the Dipartimento di Scienze della Terra of Florence (Italy); Filippo Olmi and Gloria Vaggelli for allowing access to microprobe facilities; Giordano Montegrossi for help during wet chemistry analysis; Piero Manetti for constantly supporting the research; and Jim Luhr and Alfredo Aguillón-Robles for critical and thoughtful reviews of an early draft of the manuscript. Andrea Orlando and Giulia Perini are thanked for constantly stirring discussion. Skeptical and thoughtful reviews by Rebecca Lange and Jim Gardner greatly helped to strengthen the final manuscript. Careful review by Claus Siebe improved the English style. Financial support was provided by Università degli Studi di Firenze through ex 60% grant and through a Ph.D. fellowship granted to Chiara M. Petrone, by MIUR Ministero Università e Ricerca Scientifica) funds, and by a bilateral CNR (Consiglio Nazionale delle Ricerche)-CONACyT project and the Sezione di Firenze of the Istituto di Geoscienze e Georisorse.

REFERENCES CITED

Avanzinelli, R., Conticelli, S., Francalanci, L., Manetti, P., Perini, G., Petrone, C.M., Tommasini, S., and Ulivi, M., 2001, Radiogenic isotope geology in Florence: Aims and perspective: Geoitalia 2001, Abstract volume, Cieti, Italy, p. 705–706.

Bacon, C.R., and Hirschmann, M.M., 1988, Mg/Mn partitioning as a test for equilibrium between coexisting Fe-Ti oxide: American Mineralogist, v. 73, p. 57–61.

Bence, A.E., and Albee, A.L., 1968, Empirical correction factors for the electron microanalysis of silicates and oxides: Journal of Geology, v. 76, p. 382–402.

Brey, G.P., and Köhler, T., 1990, Geothermobarometry in four phase lherzolites. II: New thermobarometers and practical assessment of using thermobarometers: Journal of Petrology, v. 31, p. 1353–1378.

Cameron, K.L., Robinson, J.V., Niemeyer, S., Nimz, G.J., Kuentz, D.C., Harmon, R.S., Bohlen, S.R., and Collerson, K.D., 1992, Contrasting styles of pre-Cenozoic and mid-Tertiary crustal evolution in northern Mexico: Evidence from deep crustal xenoliths from La Olivina: Journal of Geophysical Research, v. 97, no. B12, p. 17,353–17,376.

Carmichael, I.S.E., 2002, The andesite aqueduct perspectives on the evolution of intermediate magmatism in west-central (105–99°W) Mexico: Contributions to Mineralogy and Petrology, v. 143, p. 641–663.

Castillo, D., and De La Cruz, V., 1992, Reconocimiento estructural y volcanológico en la zona termal del Domo San Pedro Lagunillas, Nayarit, Mexico: Geofísica Internacional, v. 31, p. 407–415.

Centeno-García, E., Ruiz, J., Coney, P.J., Patchett, P.J., and Gutiérrez, F.O., 1993, Guerrero terrane of Mexico: Its role in the Southern Cordillera from new geochemical data: Geology, v. 21, p. 419–422, doi: 10.1130/0091-7613(1993)021<0419:GTOMIR>2.3.CO;2.

De Paolo, D.J., 1981, Trace element and isotopic effects of combined wall rock assimilation and fractional crystallization: Earth and Planetary Science Letters, v. 53, p. 189–202, doi: 10.1016/0012-821X(81)90153-9.

DeRemer, L.A., 1986, The geologic and chemical evolution of Volcan Tepetiltic, Nayarit, Mexico [M.S. thesis]: New Orleans, Louisiana, USA, Tulane University, 158 p.

Devey, C.V., and Cox, K.G., 1987, Relationships between crustal contamination and crystallization in continental flood basalt magmas with special reference to the Deccan Traps of Western Ghats, India: Earth and Planetary Science Letters, v. 84, p. 59–68, doi: 10.1016/0012-821X(87)90176-2.

Ferrari, L., 1995, Miocene shearing along the northern boundary of the Jalisco block and the opening of the southern Gulf of California: Geology, v. 23, p. 751–754, doi: 10.1130/0091-7613(1995)023<0751:MSATNB>2.3.CO;2.

Ferrari, L., and Rosas-Elguera, J., 2000, Late Miocene to Quaternary extension at the northern boundary of the Jalisco block, western Mexico: The Tepic-Zacoalco rift revised, *in* Delgado-Granados, H., Aguirre-Diaz, G., and Stock, J.M., eds., Cenozoic tectonics and volcanism of Mexico: Geological Society of America Special Paper 334, p. 41–64.

Ferrari, L., Pasquarè, G., Venegas-Salgado, S., and Romero-Ríos, F., 2000, Geology of the western Mexican Volcanic Belt and adjacent Sierra Madre Occidental and Jalisco block, *in* Delgado-Granados, H., Aguirre-Diaz, G., and Stock, J.M., eds., Cenozoic tectonics and volcanism of Mexico: Geological Society of America Special Paper 334, p. 65–84.

Ferrari, L., Petrone, C.M., and Francalanci, L., 2001, Generation of OIB-type volcanism in the western Trans-Mexican Volcanic Belt by slab roll-back, asthenosphere infiltration and variable flux-melting: Geology, v. 29, p. 507–510, doi: 10.1130/0091-7613(2001)029<0507:GOOIBT>2.0.CO;2.

Ferrari, L., Petrone, C.M., Francalanci, L., Tagami, T., Eguchi, M., Conticelli, S., Manetti, P., and Venegas-Salgado, S., 2003, Geology of the San Pedro–Ceboruco graben, western Trans-Mexican Volcanic Belt: Revista Mexicana de Ciencias Geológicas, v. 20, p. 165–181.

Francalanci, L., and Santo, A.P., 1993, Magmatological evolution of Filicudi volcanoes, Aeolian Islands, Italy: Constraints from mineralogical, geochemical and isotopic data: Acta Vulcanologica, v. 3, p. 203–227.

Francalanci, L., Manetti, P., Peccerillo, A., and Keller, J., 1993, Magmatological evolution of the Stromboli volcano (Aeolian Arc, Italy): Inferences from major and trace element and Sr isotopic composition of lavas and pyroclastic rocks: Acta Vulcanologica, v. 3, p. 127–151.

Franzini, M., Leoni, L., and Saitta, M., 1972, A simple method to evaluate matrix effects in X-ray fluorescence analysis: X-Ray Spectrometry, v. 1, p. 151–154, doi: 10.1002/xrs.1300010406.

Frey, H.M., Lange, R.A., Hall, C.M., and Delgado-Granados, H., 2004a, Magma eruption rate constrained by ^{40}Ar-^{39}Ar chronology and GIS for the Ceboruco–San Pedro volcanic field, western Mexico: Geological Society of America Bulletin, v. 116, p. 259–276, doi: 10.1130/B25321.1.

Frey, H.M., Lange, R.A., Hall, C.M., Nelson S., and Delgado-Granados, H., 2004b, Eruptive history of Volcán Tepetiltic, Mexico: Evidence for remelting of silicic ashflows revealed by ^{40}Ar/^{39}Ar geochronology: Eos (Transactions, American Geophysical Union), v. 85(47), Abstract V53A-0606.

Frost, B.R., and Lindsley, D.H., 1991, Occurrence of iron-titanium oxides in igneous rocks: Reviews in Mineralogy, v. 25, p. 433–468.

Gardner, J., and Tait, S., 2000, The caldera-forming eruption of Volcán Ceboruco, Mexico: Bulletin of Volcanology, v. 62, p. 20–33, doi: 10.1007/s004450050288.

Gastil, G., Krummenacher, D., and Jensky, A.W., 1978, Reconnaissance geologic map of the west-central part of the state of Nayarit, Mexico: Geological Society of America Maps and Chart Series MC-24, scale 1:200,000.

Ghiorso, M.S., and Sack, R.O., 1991, Fe-Ti oxide geothermometry: Thermodynamic formulation and the estimation of intensive variables in silicic magmas: Contributions to Mineralogy and Petrology, v. 108, p. 485–510, doi: 10.1007/BF00303452.

Holland, T., and Blundy, J., 1994, Non-ideal interactions in calcic amphiboles and their bearing on amphibole-plagioclase thermometry: Contributions to Mineralogy and Petrology, v. 116, p. 433–447, doi: 10.1007/BF00310910.

Housh, T.B., and Luhr, J.F., 1991, Plagioclase-melt equilibria in hydrous systems: American Mineralogist, v. 76, p. 477–492.

Huppert, H.E., and Sparks, R.S.J., 1985, Cooling and contamination of mafic and ultramafic magmas during ascent through the continental crust: Earth and Planetary Science Letters, v. 74, p. 371–386.

Irvine, T.N., and Baragar, W.R.A., 1971, A guide to the chemical classification of the common igneous rocks: Canadian Journal of Earth Sciences, v. 8, p. 523–548.

Jenkins, R., and De Vries, J.L., 1971, Spettrometria a raggi X in pratica: Milano, Italy, Biblioteca Tecnica Philips, 193 p.

Johnson, M.C., and Rutherford, M.J., 1989, Experimental calibration of the aluminum-in-hornblende geobarometer with application to Long Valley caldera (California) volcanic rocks: Geology, v. 17, p. 837–841.

Köhler, T.P., and Brey, G.P., 1990, Calcium exchange between olivine and clinopyroxene calibrated as a geothermobarometer for natural peridotites from 2 to 60 kb and applications: Geochimica et Cosmochimica Acta, v. 54, p. 2375–2388, doi: 10.1016/0016-7037(90)90226-B.

Leake, B.E., Woolley, A.R., Arps, C.E.S., Birch, W.D., Gilbert, M.C., Grice, K.D., Hawthorne, F.C., Kato, A., Kisch, H.J., Krivovichev, V.G., Linthout, K., Laird, J., Mandarino, J.A., Marisch, W.V., Nickel, E.H., Rock, N.M.S., Schumacher, J.C., Smith, D.C., Stephenson, N.C.N., Ungaretti, L., Whittaker, E.J.W., and Youzhi, G., 1997, Nomenclature of amphiboles: Report of the Subcommittee on Amphiboles of the International Mineralogical Association, Commission on New Mineral Names: American Mineralogist, v. 82, p. 1019–1037.

Le Bas, M.J., Le Maitre, R.W., and Woolley, A.R., 1992, The construction of the total alkali-silica chemical classification of volcanic rocks: Mineralogy and Petrology, v. 46, p. 1–22, doi: 10.1007/BF01160698.

Luhr, J., 1997, Extensional tectonics and the diverse primitive volcanic rocks in the western Mexican Volcanic Belt: Canadian Mineralogist, v. 35, p. 473–500.

Luhr, J., 2000, The geology and petrology of Volcán San Juan Nayarit, Mexico, and the compositionally zoned Tepic Pumice: Journal of Volcanology and Geothermal Research, v. 95, p. 109–156, doi: 10.1016/S0377-0273(99)00133-X.

Luhr, J.F., Allan, J.F., Carmichael, I.S.E., Nelson, S.A., and Hasenaka, T., 1989, Primitive calc-alkaline and alkaline rock types from the western Mexican Volcanic Belt: Journal of Geophysical Research, v. 94, p. 4515–4530.

Mahood, G.A., and Halliday, A.N., 1988, Generation of high-silica rhyolite: A Nd, Sr and O isotopic study of Sierra La Primavera, Mexican Volcanic Belt: Contributions to Mineralogy and Petrology, v. 100, p. 183–191, doi: 10.1007/BF00373584.

Matthews, S.J., Jones, A.P., and Gardeweg, M.C., 1994, Lascar volcano, northern Chile; evidence for steady-state disequilibrium: Journal of Petrology, v. 35, p. 401–432.

Moore, G., and Carmichael, I.S.E., 1998, The hydrous phase equilibria (to 3 kbar) of an andesite and basaltic andesite from western Mexico: Constraints on water content and conditions of phenocryst growth: Contributions to Mineralogy and Petrology, v. 130, p. 304–319, doi: 10.1007/s004100050367.

Morimoto, N., Fabries, J., Ferguson, A.K., Ginzburg, I.V., Ross, M., Seifeit, F.A., and Zussman, J., 1989, Nomenclature of pyroxenes: Canadian Mineralogist, v. 27, p. 143–156

Nelson, S.A., 1980, Geology and petrology of Volcán Ceboruco, Nayarit, Mexico: Geological Society of America Bulletin, v. 91, p. 2290–2431, doi: 10.1130/0016-7606(1980)91<639:GAPOVC>2.0.CO;2.

Nelson, S.A., and Carmichael, I.S.E., 1984, Pleistocene to Recent alkalic volcanism in the region of Sanganguey volcano, Nayarit, Mexico: Contributions to Mineralogy and Petrology, v. 85, p. 321–335, doi: 10.1007/BF01150290.

Nelson, S.A., and Livieres, R.L., 1986, Contemporaneous calc-alkaline and alkaline volcanism at Sanganguey volcano, Nayarit, Mexico: Geological Society of America Bulletin, v. 97, p. 798–808, doi: 10.1130/0016-7606(1986)97<798:CCAAVA>2.0.CO;2.

Nimis, P., 1999, Clinopyroxene geobarometry of magmatic rocks. Part 2: Structural geobarometers for basic to acid, tholeiitic and mildly alkaline magmatic systems: Contributions to Mineralogy and Petrology, v. 135, p. 62–74, doi: 10.1007/s004100050498.

Peccerillo, A., and Wu, T.W., 1992, Evolution of calc-alkaline magmas in continental arc volcanoes: Evidence from Alicudi, Aeolian arc (southern Tyrrhenian Sea, Italy): Journal of Petrology, v. 33, p. 1295–1315.

Petrone, C.M., Tagami, T., Francalanci, L., Matsumura, A., and Sudo, M., 2001, Volcanic systems in the San Pedro–Ceboruco graben (Nayarit, Mexico) in the light of new K-Ar geochronological data: Geochemical Journal, v. 35, p. 77–88.

Petrone, C.M., Francalanci, L., Carlson, R.W., Ferrari, L., and Conticelli, S., 2003, Unusual coexistence of subduction-related and intraplate-type magmatism: Sr, Nd and Pb isotope and trace element data from the magmatism of the San Pedro–Ceboruco graben (Nayarit, Mexico): Chemical Geology, v. 193, p. 1–24, doi: 10.1016/S0009-2541(02)00229-2.

Poli, G., Manetti, P., Peccerillo, A., and Cecchi, A., 1977, Determinazione di alcuni elementi del gruppo delle terre rare in rocce silicatiche per attivazione neutronica: Rendiconti Società Italiana Mineralogia e Petrologia, v. 33, p. 755–763.

Righter, K., Carmichael, I.S.E., Becker, T.A., and Renne, R.P., 1995, Pliocene to Quaternary volcanism and tectonism at the intersection of the Mexican Volcanic Belt and the Gulf of California: Geological Society of America Bulletin, v. 107, p. 612–626, doi: 10.1130/0016-7606(1995)107<0612:PQVAFA>2.3.CO;2.

Rosas-Elguera, J., Ferrari, L., Garduño-Monroy, V.H., and Urrutia-Fucugauchi, J., 1996, Continental boundaries of the Jalisco block and their influence in the Pliocene-Quaternary kinematics of western Mexico: Geology, v. 24, p. 921–924, doi: 10.1130/0091-7613(1996)024<0921:CBOTJB>2.3.CO;2.

Ruiz, J., Patchett, P.J., and Arculus, R.J., 1988, Nd-Sr isotope composition of lower crustal xenoliths: Evidence for the origin of mid-Tertiary felsic volcanism in Mexico: Contributions to Mineralogy and Petrology, v. 99, p. 36–43, doi: 10.1007/BF00399363.

Saunders, A.D., 1982, Geochemistry of basalts recovered from the Gulf of California during Leg 65 of the Deep Sea Drilling Project, *in* Lewis, B.T.R., Robinson, P., et al., Initial Reports, Deep Sea Drilling Project Leg 65: Washington, D.C., U.S. Government Printing Office, p. 591–621.

Schaaf, P., Böhnel, H., and Pérez-Venzor, J.A., 2000, Pre-Miocene paleogeography of the Los Cabos block, Baja California Sur: Geochronological and paleomagnetic constraints: Tectonophysics, v. 318, p. 53–69, doi: 10.1016/S0040-1951(99)00306-6.

Schaaf, P., Hall, B.V., and Bissig, T., 2003, The Puerto Vallarta batholith and Cuale mining district, Jalisco, Mexico—High diversity parenthood of continental arc magmas and Kuroko-type volcanogenic massive sulfide deposits, *in* Morán Zenteno, D., ed., Geologic transects across Cordilleran Mexico: Instituto de Geología, Universidad Nacional Autónoma de México (UNAM) Special Publication 1, p. 183–200.

Schmitt, A.K., de Silva, S.L., Trumbull, R.B., and Emmermann, R., 2001, Magma evolution in the Purico ignimbrite complex, northern Chile: Evidence for zoning of a dacitic magma by injection of rhyolitic melts following mafic recharge: Contributions to Mineralogy and Petrology, v. 140, p. 680–700.

Smith, A.D., 1999, The Nd-Sr-Pb isotopic record in abyssal tholeiites from the Gulf of California region, western Mexico: No evidence for a gulf mouth plume: International Geology Review, v. 41, p. 921–931.

Spencer, K.J., and Lindsley, D.H., 1981, A solution model for coexisting iron-titanium oxides: American Mineralogist, v. 66, p. 1189–1201.

Sun, S.S., and McDonough, W.F., 1989, Chemical and isotopic systematics of oceanic basalts: Implications for mantle composition and processes, *in* Saunders, A.D., and Norry, M.J., eds., Magmatism in the ocean basins: Geological Society of America Special Paper 42, p. 313–346.

Urrutia-Fucugauchi, J., and Flores-Ruiz, J.H., 1996, Bouguer gravity anomalies and regional crustal structure in central Mexico: International Geology Review, v. 38, p. 176–194.

Vaggelli, G., Olmi, F., and Conticelli, S., 1999, Quantitative electron microprobe analyses of reference silicate mineral and glass samples: Acta Vulcanologica, v. 11, p. 297–303.

Venezky, D.Y., and Rutherford, M.J., 1999, Petrology and Fe-Ti oxide reequilibration of the 1991 Mount Unzen mixed magma: Journal of Volcanology and Geothermal Research, v. 89, p. 213–230, doi: 10.1016/S0377-0273(98)00133-4.

Verma, S.P., and Nelson, S.A., 1989a, Isotopic and trace element constraints on the origin and evolution of alkaline and calc-alkaline magmas in the north-western Mexican Volcanic Belt: Journal of Geophysical Research, v. 94, no. B4, p. 4531–4544.

Verma, S.P., and Nelson, S.A., 1989b, Correction to “Isotopic and trace element constraints on the origin and evolution of alkaline and calc-alkaline magmas in the north-western Mexican Volcanic Belt”: Journal of Geophysical Research, v. 96, no. B6, p. 7679–7681.

Wallace, P., and Carmichael, I.S.E., 1994, Petrology of Volcán Tequila, Jalisco, Mexico: Disequilibrium phenocryst assemblages and evolution of the subvolcanic magma system: Contributions to Mineralogy and Petrology, v. 117, p. 345–361, doi: 10.1007/BF00307270.

MANUSCRIPT ACCEPTED BY THE SOCIETY 28 JULY 2005

Printed in the USA

Downloaded from specialpapers.gsapubs.org on July 1, 2015

Geological Society of America Special Papers

The San Pedro–Cerro Grande volcanic complex (Nayarit, México): Inferences on volcanology and magma evolution

Chiara M. Petrone, Lorella Francalanci, Luca Ferrari, et al.

Geological Society of America Special Papers 2006;402; 65-98
doi:10.1130/2006.2402(03)

E-mail alerting services	click www.gsapubs.org/cgi/alerts to receive free e-mail alerts when new articles cite this article
Subscribe	click www.gsapubs.org/subscriptions to subscribe to Geological Society of America Special Papers
Permission request	click www.geosociety.org/pubs/copyrt.htm#gsa to contact GSA.

Copyright not claimed on content prepared wholly by U.S. government employees within scope of their employment. Individual scientists are hereby granted permission, without fees or further requests to GSA, to use a single figure, a single table, and/or a brief paragraph of text in subsequent works and to make unlimited copies of items in GSA's journals for noncommercial use in classrooms to further education and science. This file may not be posted to any Web site, but authors may post the abstracts only of their articles on their own or their organization's Web site providing the posting includes a reference to the article's full citation. GSA provides this and other forums for the presentation of diverse opinions and positions by scientists worldwide, regardless of their race, citizenship, gender, religion, or political viewpoint. Opinions presented in this publication do not reflect official positions of the Society.

Notes

Geological Society of America

THE
GEOLOGICAL
SOCIETY
OF AMERICA